Fundamental Toxicology Studies of 2D Transition Metal Dichalcogenides

by

Michael Tran

A Thesis Presented in Partial Fulfillment
of the Requirements for the Degree
Master of Science

Approved November 2019 by the
Graduate Supervisory Committee:

Sefaattin Tongay, Co-Chair
Matthew Green, Co-Chair
Christopher Muhich

ARIZONA STATE UNIVERSITY

December 2019

ABSTRACT

Two-dimensional quantum materials have garnered increasing interest in a wide variety of applications due to their promising optical and electronic properties. These quantum materials are highly anticipated to make transformative quantum sensors and biosensors. Biosensors are currently considered among one of the most promising solutions to a wide variety of biomedical and environmental problems including highly sensitive and selective detection of difficult pathogens, toxins, and biomolecules. However, scientists face enormous challenges in achieving these goals with current technologies. Quantum biosensors can have detection with extraordinary sensitivity and selectivity through manipulation of their quantum states, offering extraordinary properties that cannot be attained with traditional materials. These quantum materials are anticipated to make significant impact in the detection, diagnosis, and treatment of many diseases.

Despite the exciting promise of these cutting-edge technologies, it is largely unknown what the inherent toxicity and biocompatibility of two-dimensional (2D) materials are. Studies are greatly needed to lay the foundation for understanding the interactions between quantum materials and biosystems. This work introduces a new method to continuously monitor the cell proliferation and toxicity behavior of 2D materials. The cell viability and toxicity measurements coupled with Live/Dead fluorescence imaging suggest the biocompatibility of crystalline MoS_2 and MoSSe monolayers and the significantly-reduced cellular growth of defected $MoTe_2$ thin films and exfoliated MoS_2 nanosheets. Results show the exciting potential of incorporating kinetic cell viability data of 2D materials with other assay tools to further fundamental understanding of 2D material biocompatibility.

ACKNOWLEDGMENTS

I would like to express my most sincere gratitude to my advisors, Prof. Sefaattin Tongay and Prof. Matthew Green. They have shown incredible patience, enthusiasm, wisdom, and endless support in my Master's study. Their intense passion and commitment to their work has motivated me to give my best effort into my research. I could have not asked for more encouraging and caring advisors as my mentors at Arizona State University.

I would also like to thank Prof. Christopher Muhich for serving as my committee member and his valuable contributions to this thesis. My sincere thanks go to Dr. Page Belauch for all the training, advice, and resources she has supported me through my research. I would like to also thank every one of my lab members, for all their guidance and contributions in my research. Their work ethic and intense desire to discover new materials has continuously inspired me every day at the lab. This journey was made more enjoyable and productive with everyone.

I want to thank my parents and family for their unconditional support throughout my life that has made this work possible. Special thanks to Caitlin Jomoc for all her love and support.

TABLE OF CONTENTS

Page

CHAPTER Page

CHAPTER Page

LIST OF FIGURES

Figure Page

Figure Page

Figure Page

CHAPTER 1

INTRODUCTION

1.1 Two-Dimensional (2D) Materials

The future of microelectronics and nanotechnology relies upon the miniaturization of advanced materials. Internet of Things, portable bio-electronics, quantum computing, and many other challenging technologies require stronger and smaller devices with increasing functionalities.[1] A rapidly growing class of materials holds promise to unlock the necessary electrical, mechanical, and optical properties for these applications. Two-dimensional materials, also referred to as layered materials, are crystalline materials consisting of single sheets that are a unit cell thick and weakly coupled by van Der Waals interactions. Since the interlayer interactions are much weaker than the in-plane atomic bonds, the sheets can be separated with techniques such as mechanical or liquid exfoliation. As the crystal is reduced to nano- or atomic-scale thickness, the quantum size effect occurs, resulting in interesting physical, electronic, and optical properties that are significantly different from their bulk counterparts.

This class of materials has garnered tremendous interest since the successful exfoliation of single layer graphene from graphite in 2004 by A. Geim and K. Novoselov.[2] Graphene's superior mechanical properties and exceptional electronic properties have captivated scientists all over the world, and there is a rush to realize commercial products by the industry.

However, there are many limitations to graphene that have led to intensive research into other 2D materials with different desired properties. Many other layered materials have been theorized to be stable across the periodic table. Up to 1,825

experimentally known layered bulk compounds have been identified to be able to be exfoliated through vigorous density functional theory calculations.[3] In recent years, various 2D materials have been experimentally discovered including planar analogs of graphene (silicene, phosphorene, hexagaonal boron nitride, germanene), transition metal monochalcogenides and dichalcogenides, layered perovskites, and 2D organic polymers.[4–10] These materials exhibited a wide variety of properties and potential applications. In the following sections, several notable 2D materials will be briefly introduced.

1.1.a Graphene

Although many 2D materials have been since discovered, graphene remains one of the world's most popular and intriguing material. Graphene is a crystalline 2D allotrope of carbon atoms with sp^2 hybridization to form a hexagonal lattice. Like most layered materials, graphene can be synthesized from top-down methods, such as liquid or mechanical exfoliation, and bottom-up methods, such as chemical vapor deposition (CVD).[11]

Compared to its bulk graphite, graphene has many desirable physical and electronic properties that can open up pathways to a wide variety of applications. A single sheet of graphene possesses extraordinary mechanical properties due to the stability of the sp^2 bonds which greatly opposes a variety of in-plane deformations. A defect-free monolayer membrane measured an intrinsic strength of 42 Nm^{-1} and a Young's Modulus of 1 TPa, which is many times stronger and lighter than steel.[12] The incorporation of graphene particles into nanocomposites has demonstrated significant

enhancement to their mechanical properties due to its high aspect ratio and intrinsic mechanical strength.[13]

Along with its excellent mechanical properties, graphene is a zero-band gap semiconductor with high intrinsic electron mobility, electronic conductivity, optical transmittance, and thermal conductivity. These unique properties can allow for the potential advancement of transparent electronics, field-effect transistors, energy storage, bio-sensors, and water filtration technologies.[14–18] Although there are many possible applications with graphene, its lack of a band gap severely limits its use in electronic switch control since a band gap allows for control and manipulation of electron flow in electronics. There have been recent developments in strain engineering, chemical functionalization, and manipulation of graphene architectures to widen the band gap.[19–21] Even with these efforts, the lack of a wider band gap have directed researchers into investigating other 2D materials with semiconducting character.

1.1.b Transition Metal Dichalcogenides (TMDCs)

2D Transition metal dichalcogenides are promising alternatives to graphene. They follow the stoichiometric formula, MX_2, where M is a transition metal atom from group IV (Ti, Zr, or Hf), group V (V, Nb, or Ta) or group Vi (Mo or W) and X is a chalcogen (S, Se, or Te). TMDCs are layered materials which can be mechanically exfoliated to single sheets due to the weak interlayer van Der Waals interactions or synthesized from chemical vapor deposition. In monolayer form, many of these materials exhibit a direct bandgap, strong spin-orbit coupling, and favorable electronic and mechanical properties.[22]

The diverse selection of 2D TMDCs offer exciting possibilities with its tunable electronic structures. Depending on the elemental compositions, these materials can exhibit semiconducting (MoS_2, WS_2, etc.) or metallic behavior (VSe2, NbS2, etc.).[22] Due to the quantum confinement effect, the band structure of these 2D materials can be tuned as the number of layers shrinks down. For example, the MoX_2 and WX_2 class TMDCs exhibit a widening of the band gap with decreasing atomic thickness and, ultimately, a transition from an indirect band gap to a direct band gap in the monolayer limit. Recent studies have demonstrated the promise of 2D TMDCs through the developments of nanoscale field-effect transistors, photonics, sensing, energy storage, and opto-electronics.[23–27] The electronic and optical properties of TMDCs can be further manipulated with strain engineering, defect engineering, doping, alloying, synthesis of Janus particles, and careful design of heterostructures.[28–33] In this section, the popular MoX_2 family will be discussed.

One of the most popular 2D materials behind graphene is MoS_2. MoS_2 is an inorganic layered material that can be naturally found as a mineral ore. Each plane of Mo atoms is covalently sandwiched by sulfide atoms in a sequence of S-Mo-S with an average molecular thickness of 0.65 nm. The basic crystal structure of 2D MoS_2 consists of the trigonal prismatic structure with hexagonal (2H) symmetry, resulting in a semiconducting character. An additional meta-stable phase with octahedral coordination and tetragonal symmetry was discovered to be metallic (1T). The two phases are illustrate in Fig. 1-1a. Bulk MoS_2 has an indirect band-gap of 1.23 eV in the center of the Bruillion zone while single layer form transitions into a direct band gap of approximately 1.8 eV located at the K positions, as shown in Fig. 1-1b.[34]

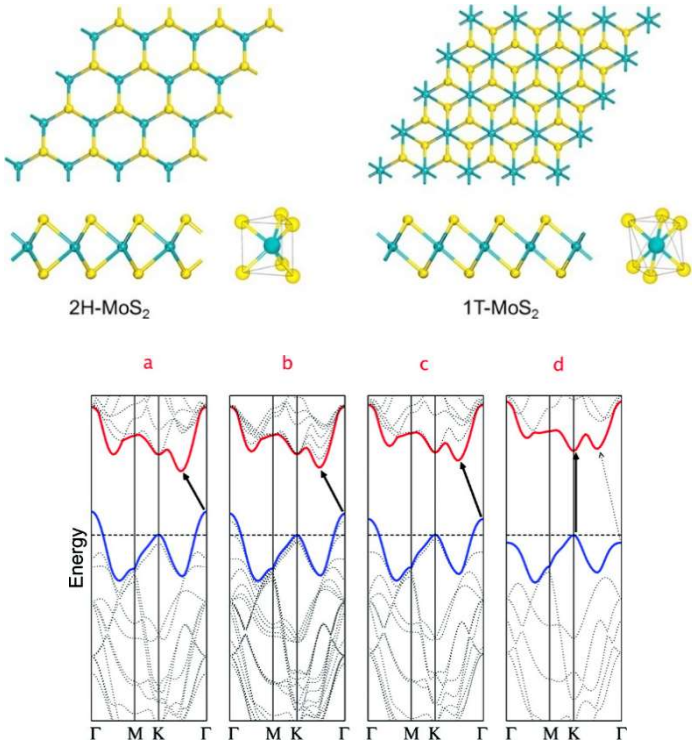

Figure 1-1 a) Schematic of MoS_2 monolayer structure and bulk unit cell[35] b) From left to right, the calculated band structures of bulk, quadrilayer, bilayer, and monolayer MoS_2[36]

$MoSe_2$ is another layered material with similar crystal and band structure to MoS_2. The crystal consists of either an octahedral or trigonal prismatic structure with Mo atoms sandwiched between Se atoms. Unlike MoS_2, bulk $MoSe_2$ is rare in nature and can be synthesized through chemical vapor transport. The sheets can then be mechanical/chemically exfoliated or directly synthesized from chemical vapor deposition. The band gap of $MoSe_2$ is lower in comparison to MoS_2, with an indirect band gap of 1.1 eV for bulk crystals and a direct band gap of 1.55 eV, resulting in high photoluminescence for single layers.[37] $MoSe_2$ offers the advantages of increased electrical conductivity and a lower band gap in the IR spectrum.

$MoTe_2$ is the final layered material from layered MoX_2 family. It commonly exists in three crystalline structures: hexagonal, monoclinic, and orthorhombic with a Mo

atom sandwiched by two Te ions. Bulk $MoTe_2$ is a semiconductor with an indirect band gap of approximately 1.0 eV. The monolayer undergoes a transition to a direct-gap semiconductor with an optical band gap of 1.1 eV with intense photoluminescence.[38] $MoTe_2$ monolayers have the preferred band gap in the lower IR spectrum but manufacturing of larger single layer crystals remains challenging.

The unique properties of the class MoX_2 include a mechanical flexibility, a direct band gap, good mobility, high current on/off ratio, large optical absorption, and a large photoluminescence peak allowing them to be used in electronics as transistors and in optics as photo-emitters or sensors.[39] They possess strong spin-orbit interactions and lack an inversion symmetry, making them attractive candidates for valleytronic and spintronic applications.

A new and exciting class of 2D materials are Janus crystals due to the breaking of the out-of-plane symmetry structure. Janus TMDC monolayers contain an asymmetric structure of MXY where (M = Mo or W, and X/Y = S, Se, or Te). Although these materials are not known to exist in nature, phonon dispersion and molecular dynamics calculations have supported the theoretical stability of MoSSe, WSSe, WSeTe, and WSTe monolayers.[40] MoSSe monolayers have been the only 2D Janus TMDCs synthesized to this date.[32] Due to the different atomic radii and electron negativity of the X and Y chalcogen elements, the charge distributions become nonuniform creating an out-of-plane polarity that causes a piezoelectric effect. 2D piezoelectric materials can offer potential applications in energy harvesting technology, nano-actuators, strain-tuned electronics and optoelectronics.[41] Janus MoSSe has also been considered as excellent materials for photocatalysis, strain-sensitive gas sensors, and electrocatalysis.[42–44] In

addition, Janus monolayers display strong Rashba spin splitting.[33] The Rashba effect is the momentum-dependent splitting of bands in asymmetric 2D materials for possible applications in spintronics.

1.2 Toxicology of 2D Materials

The scientific and industrial interest in 2D materials have been growing at a rapid pace. Figure 1-2 is a year-wise citation list of publications that have referenced "2D materials", showing the increasing trend of studying these materials. Most of the research is focused on studying the synthesis, properties, and potential applications. The diversity of 2D materials allow for wide range of applications, especially in the biomedical field.[45] Their high surface area to volume ratio, chemical reactivity, and desirable optical properties allow development of materials of drug delivery, biosensing, biomedical imaging, and photothermal therapy.

Specifically, 2D quantum biosensors can open opportunities of detecting pathogens, pathogens, toxins, and other biomarkers for diseases with the highest sensitivity, selectivity, and cost-effectiveness. Their unique and discrete quantum properties enable measurements beyond what classical sensors can do. Despite the potential of 2D materials in biological and environmental applications, there have been a severe lack of studies investigating their inherent toxicity and biocompatibility. The proactive study of the biological and environmental interactions of 2D materials will enable us to assess the material synthesis and product risks as well as deeper fundamental understanding for further biomedical applications development.

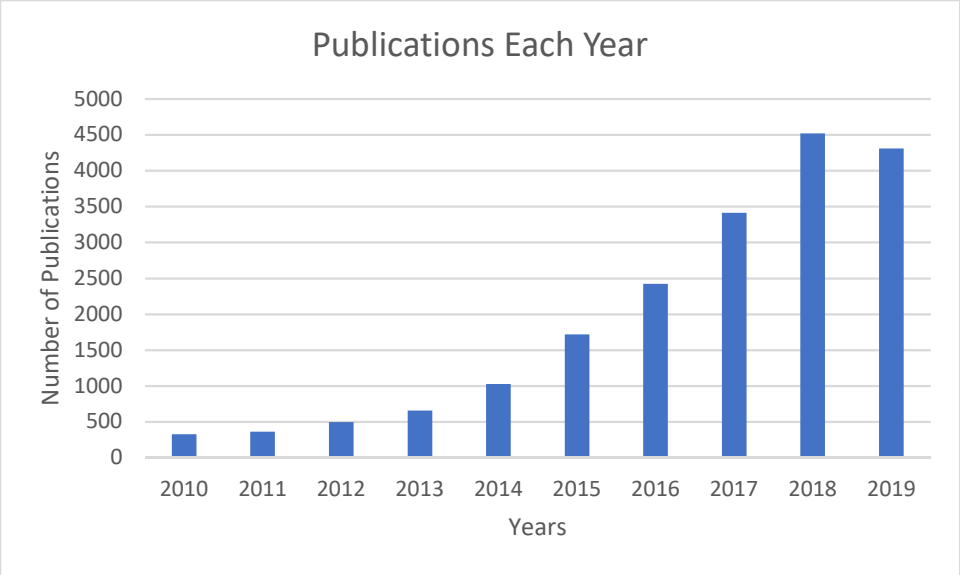

Figure 1-2 A citation report generated by a SciFinder search for "2D materials" from 2010 to present

There have been several review articles summarizing the recent publications regarding the toxicity of 2D materials, especially regarding graphene, MoS_2, and hexagonal boron nitride.[46–49] In three similar studies, the toxicity of chemically exfoliated MoS_2, WS_2, and WSe_2, VTe_2, VSe_2, VTe_2, $NbTe_2$, and TaTe2 with A549 human lung carcinoma cells was investigated at varying dosages.[50–52] After 24 hours, their cell viability and cytotoxicity results expressed increased toxicity of Se and Te chalcogens. In those studies, $NbTe_2$ and $TaTe_2$ showed higher toxicity than VTe_2, demonstrating the metal's role in cell viability as well. Several studies have also concluded increased exfoliation of MoS_2 had a greater cytotoxic effect while CVD grown MoS_2 had negligible effect on cell viability.[53,54] This and other published studies have laid the groundwork for suggesting biocompatibility of 2D materials are dependent on its chemical composition, lateral size and thickness, and morphology. It becomes increasingly important that these

characteristics as well has mode of synthesis is sufficiently analyzed before probing of their biocompatibility.

Despite the increased interest in the toxicology of 2D materials, additional fundamental understanding and investigation of 2D materials is necessary as the field and interest in biotechnology continues to grow. Many of the studies have focused on end point measurements of cell viability and cytotoxicity without answering several important fundamental questions: What interactions are happening between the cells and 2D material in between the 24 or 48 hours? How quickly are the cells growing or dying in these conditions? This study will introduce a new approach through kinetic monitoring of the cell viability and cytotoxicity in order to further lay the foundation for studying the interactions between 2D quantum materials and biosystems

CHAPTER 2

REVIEW OF EXPERIMENTAL METHODS

2.1 Crystal Growth and Sample Preparation Methodologies

2.1.a Sample Preparation Procedure

Careful sample preparation is an important factor in encouraging nucleation and crystal quality. Studies have shown that cleaner substrates, equipment, and reagents produced higher quality monolayers and thin films.[55] Sapphire substrates were selected in favor of silicon dioxide (SiO_2) substrates in the growth of the 2D MoX_2 materials due to SiO_2 degradation in Phosphate Buffer Solution (PBS).[56] The sapphire substrate was placed under a simple, yet effective cleaning procedure to remove all residues and increase surface energy for nucleation. This process involved bath sonication in acetone and isopropanol followed by blowing with dry nitrogen gas. The final step involves oxygen plasma cleaning to remove any residual contaminants.

2.1.b Chemical Vapor Deposition (CVD)

CVD is a widely-used materials fabrication technique used in both academia and industry. The majority of its applications involves the deposition or coating of solid films to surfaces, but this technique has been adapted to synthesized 2D monolayer flakes and films.[57] In general, the process involves the introduction of precursor gases into the chamber containing a heated substrate. The gas molecules will then react or decompose onto the substrate surface to produce the desired materials. Volatile byproducts and excess precursor gases are continuously evacuated by gas flow out of the reaction chamber.

The growth of monolayer TMDCs requires the precise control of many different factors including type of substrate, precursor concentration and ratio, type and flow rate of carrier gas, temperature of substrate and precursor, and pressure. There have been many studies done to understand the growth mechanisms and optimization parameters for 2D TMDCs growth.[58–60] A schematic of the atmospheric CVD set-up used in this lab is shown below in Figure 2-1.

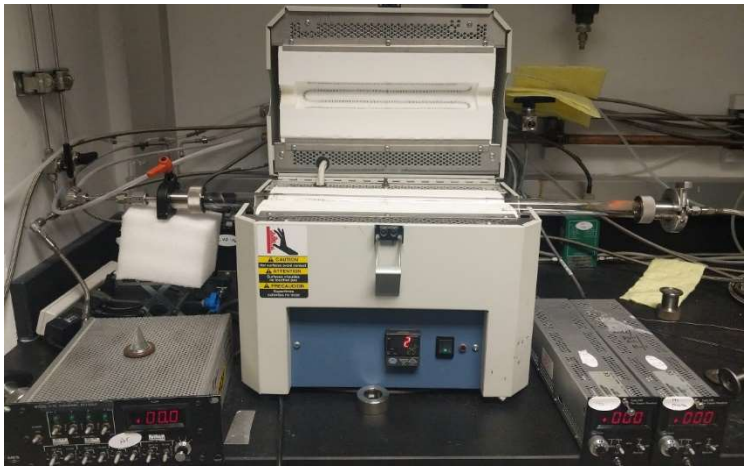

Figure 2-1 CVD set-up used in this lab

2.1.c Molecular Beam Epitaxy (MBE)

MBE is an atomic epitaxial growth technique suited for preparation of highly controlled and advanced thin film structures. The process is based on the reaction of molecular or atomic beams onto a heated substrate under an ultra-high vacuum environment. Electron-beam evaporators (K-cells) of the ultra-pure sample precursors are sublimed to create a unidirectional flow of atoms or molecules without collisions onto the substrate to react. The molecules deposit onto the surface, condense, and build up systematically into thin layers. A reflection high-energy electron diffraction equipment is attached and monitors the growth of the crystal layers in-situ. MBE allows for precise

control of elemental composition, growth conditions, purity, and in-situ growth kinetic monitoring to allow for materials engineering of high quality and complex nanostructures. A simple schematic of an MBE set-up is shown in Figure 2-2. Successful epitaxial growth of several 2D TMDCs have been reported.[61–63]

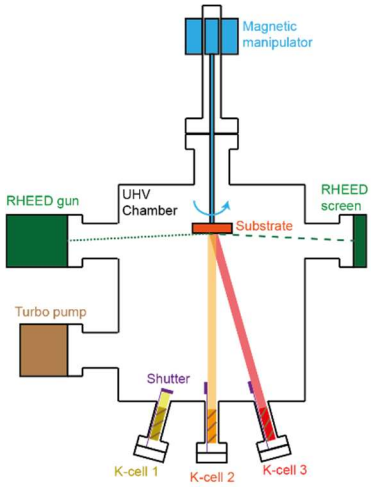

Figure 2-2 Simplified schematic of an MBE chamber

2.1.d Plasma-assisted Surface Stripping

Plasma-enhanced chemical vapor deposition (PECVD) is a type of CVD process where the activation energy of the chemical reaction is significantly lowered due to the introduction of the reactant gases as an energized plasma. Typically performed at low atmospheric pressures, the plasma is formed in an electric RF field in which the gases become ionized and highly reactive. This creates advantages of low temperature synthesis, shorter growth rates, and more direct control over growth parameters.[64]

A modified form of PECVD, plasma-assisted surface stripping process, was developed in order to synthesis 2D Janus TMDC crystals. The set-up is shown in Figure 2-3. In this process, H_2 gas is flown through the system with an attached vacuum system and the pressure is maintained at 300 mTorr. The inlet gas (H_2) is energized by an RF

generator through the coils to create highly reactive hydrogen plasma, which is shown with the purple hue. The substrates with CVD grown 2D TMDCs are placed inside tube by the tail end of the plasma gas, which is displayed as the violet hue. The Y chalcogen precursor is placed slightly upstream of the substrates. The energetic hydrogen ions travelled through the tube to strip off the exposed chalcogen of the 2D TMDCs, leaving a single layer of MX with the opposite chalcogen remaining. Simultaneously, the Y ions are transported with the energetic H_2 ions and reacts with the MX to form 2D MXY Janus crystals.

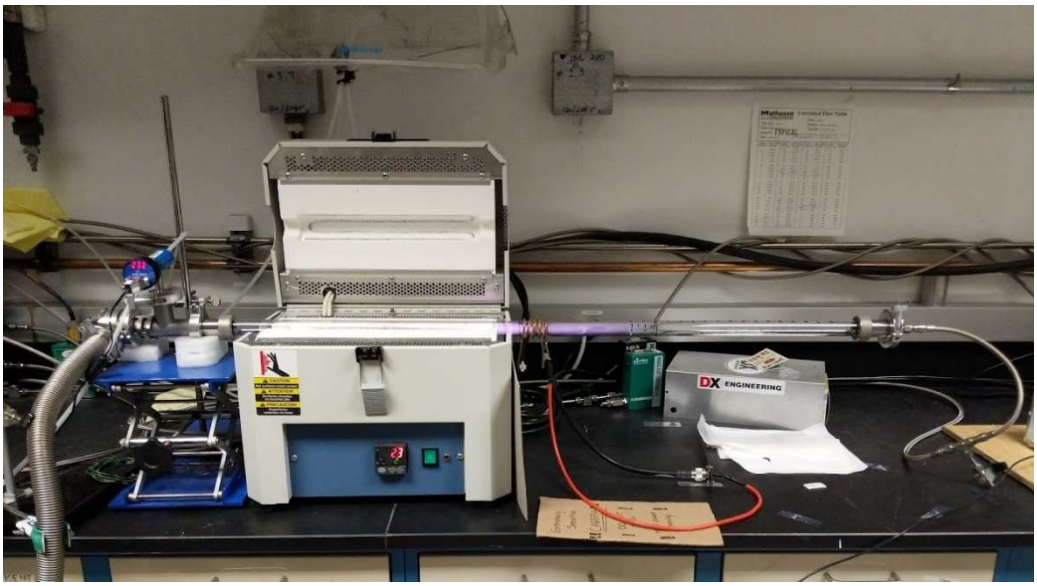

Figure 2-3 Plasma-assisted surface stripping set-up used to grow 2D Janus crystals

2.1.e Liquid Phase Exfoliation (LPE)

Since the discovery of graphene through micromechanical exfoliation of graphite, this technique has been successfully adapted to many other layered materials to produce highly crystalline sheets. However, one of the biggest drawbacks is the limitation of the sizes and quantities of 2D materials produced. LPE is an attractive alternative for the scalable production of large quantities of 2D nanosheets. This method applies high shear

or ultrasound energy to layered crystals in stabilizing liquid solutions to produce thin nanosheets.

Efficient exfoliation of layered materials can be considered as a three-step process, as shown in Figure 2-4a. The solvent molecules must be able to immerse itself in between the layered sheets, followed by energetic separation of the flakes, and stabilization of the sheets to prevent restacking. A multitude of factors will determine the effectiveness of the exfoliation. Coleman et al. provides a detailed guide to LPE of layered materials, listing out important factors that include solvent choice, type of sonication (probe vs bath), sonication power, initial concentration, duration of sonication, and total volume.[65] Efficient dissolution and stabilization can be optimized by matching the surface energies and solubility parameters of the solution and layered crystals. In this study, the co-solvent of isopropyl alcohol (IPA) and deionized (DI) water was selected the LPE of MoS_2. Traditional organic solvents such as N-Methyl-2-pyrrolidone was not used due to their toxicity and difficulty in post-exfoliation removal. A mixture of 70% isopropyl alcohol (IPA) and 30% deionized (DI) water by volume was decided due to proven effective exfoliation and stability studies based on matching surface energies.[66] Probe sonication is used for these experiments instead of bath sonication due to the higher output energy for a more efficient exfoliation..

LPE produces polydisperse flakes mixed in with unexfoliated bulk crystals. To remove the original starting material and larger flakes, liquid cascade centrifugation is employed for size selection. Size selection of nanomaterials can be performed with centrifugation where the thinner sheets will reside in the supernatant and thicker flakes will settle in the sediment. This cycle can be repeated to isolate thinner materials, albeit at

lower concentrations for each cycle. A faster rotational speed will also result in better separation of thinner flakes. An example of the liquid cascade centrifugation process is shown below in Figure 2-4b.

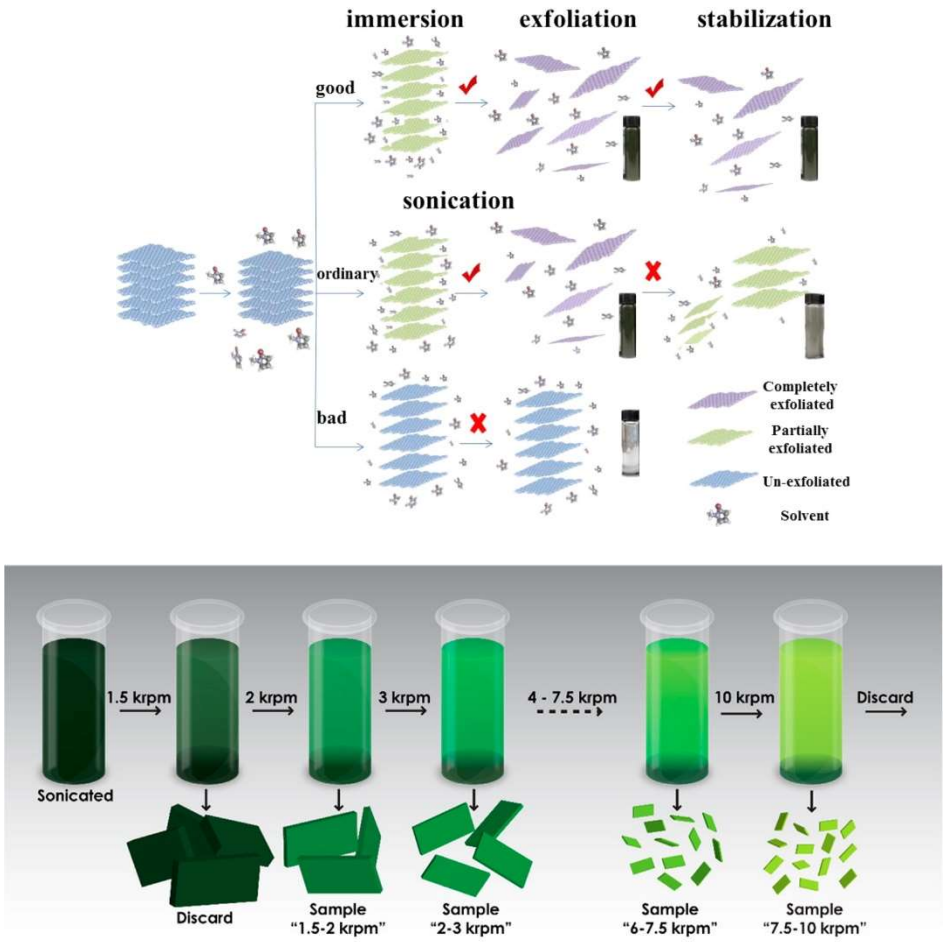

Figure 2-4. a) Mechanism behind LPE process[67] b) Example of liquid cascade centrifugation process[68]

2.2 Sample Characterization Methodologies

After crystal growth and sample preparation, various characterization techniques were employed to identify the 2D material, its crystallinity, thickness, and morphology. Raman spectroscopy, photoluminescence spectroscopy, and atomic force microscopy were utilized to analyze the properties. As briefly mentioned in the introduction, the

physical properties and structure of the 2D material may have significant effect on the toxicity and sufficient characterization is necessary to properly investigate their biocompatibility. In this section, a brief overview of each technique will be introduced.

2.2.a Raman Spectroscopy

Raman spectroscopy is a non-destructive analysis technique that provides the specific fingerprint to identify materials through the analysis of their vibrational modes. In addition, it can be used to analyze the crystallinity, orientation, presence of defects, thickness and strain of materials. The wealth of information this method provides makes it a staple characterization tool for 2D materials.

The principle behind Raman scattering and typical spectroscopic set-up is shown in Figure 2-5. When a sample is irradiated with a monochromatic source of light, there are light-matter interactions that will result in reflected, absorbed, or scattered light. Scattered light can be separated into elastic and inelastic scattering. Elastic scattering is the dominating process and occurs when the photons interact with the material and retain their original energy state. This is called Rayleigh scattering and is typically filtered out of the spectrometer. For inelastic scattering, a small portion of the scattered light interacts with the material and exchanges energy. This exchange of energy results in two different inelastic scattering mechanisms, Stokes and Anti-stokes scattering. Anti-stokes Raman scattering occurs when the molecular vibration of the molecule transfers to the photon; however, this process is energetically less likely to occur and generally not collected. In Stokes scattering, the incident photons lose a portion of their energy to lattice vibrations. The amount of energy transferred to excite the vibrational mode (phonons) is exact and this information is collected through a charged coupled detector to generate a plot

showing peak intensity against wavenumber (cm^{-1}). The location, intensity, and their full width at half maximum (FWHM) can provide information on the identity, crystallinity, and relative quantity of the material.

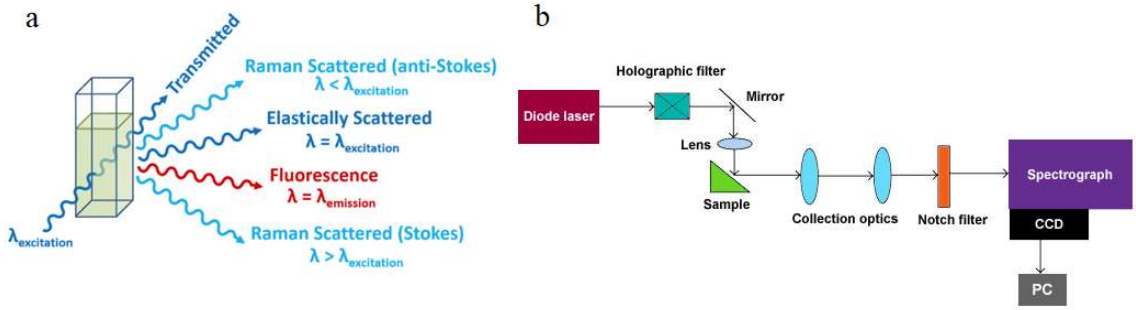

Figure 2-5 a) Schematic identifying the light scattering mechanisms after laser exposure to sample[69] b) Schematic of general Raman set-up[70]

2.2.b Photoluminescence Spectroscopy (PL)

PL is another non-destructive and non-contact characterization tool that is usually coupled with Raman spectroscopy. It is a form of light emission that occurs during the recombination photo-excited electron-hole pairs. The underlying mechanism and physics of PL is highlighted in Figure 2-6. The process begins with an irradiated laser beam incident on the sample. Light with energy greater than the material's band gap will excite electrons from the valence band to the conduction band. The relaxation of the excited electron back to the valence band products an emission of light captured by a CCD detector.

The produced PL spectra can provide a variety of information regarding the material's optical properties, crystallinity, thickness, and defect concentration. In a direct bandgap semiconductor like monolayer MoS_2, the PL spectrum can determine the intrinsic optical bandgap since the recombination is a very efficient process. Indirect

band gap materials will not produce efficient PL peaks since the relaxation of photoexcited electrons requires non-radiative recombination processes due to the momentum difference of the valence band maxima and conduction band minima. Because of these two underlying mechanisms, PL is an excellent technique to study 2D TMDCs since their monolayers have a direct band gap and their bulk counterparts possess indirect band gaps. The crystallinity, thickness, and concentration of defects can be determined by comparing the spectrum to established defect-free single layer TMDCs PL spectrums.

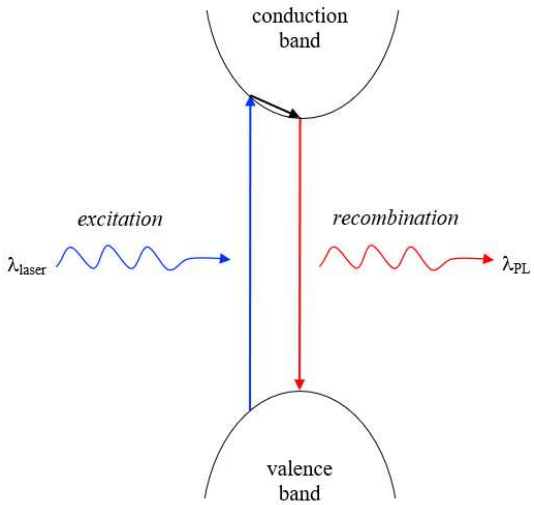

Figure 2-6 Schematic of photoluminescence mechanism

2.2.c Atomic Force Microscopy (AFM)

AFM is a microscopy technique that can perform surface characterization of most flat materials at nanoscale resolution. This tool with slight modifications can be used for imaging of material topography, phase change, thickness, thermal and electrical conductivity, magnetism, and piezoelectric behavior. A typical AFM set-up is shown in Figure 2-7. In our AFM system, a piezoelectric scanner controls the cantilever and probe.

The cantilever has a reflective coating on the topside that reflects light, which is detected by a photodiode. As the tip moves across the sample, the cantilever moves vertically up and down due to the local forces between the tip and sample. The reflected light mirrors the cantilever motion, and the signal is recorded by the detector. The topography of the surface can be imaged by raster scanning of the sample and recording of the probe height while holding the signal of the probe-sample interaction constant. AFM can operate in contact, tapping, or non-contact mode. Generally, tapping and non-contact modes are preferable on softer materials but may produce lower lateral resolution images.

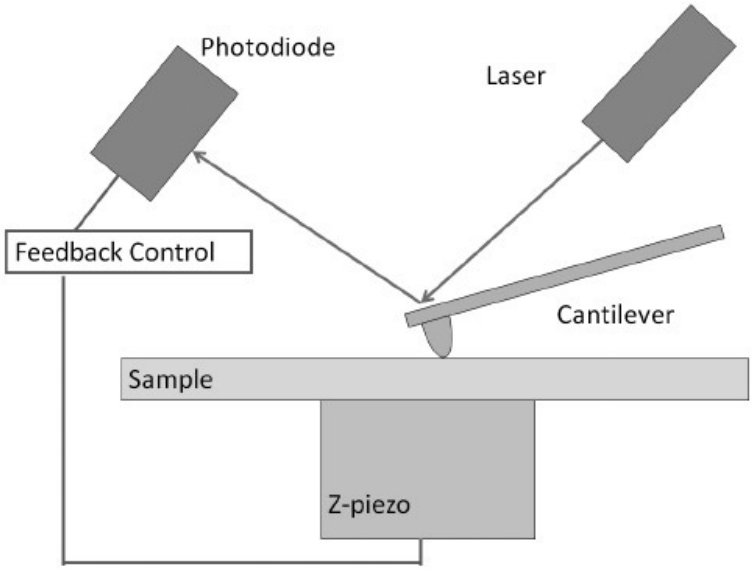

Figure 2-7 Typical AFM set-up[71]

2.3 Toxicology Methodology

As mentioned in Chapter 1, there is a need for investigating and understanding the interaction between 2D materials and cells. The following section will highlight the techniques used in preparing cells and characterizing their surface interactions with various 2D TMDCs.

2.3.a Cells and Cell Culturing

NIH 3T3 cells were used in the following toxicology measurements. This immortal cell line originated from primary mouse embryonic fibroblast cells with an average doubling time of 20-26 hours. These cells are adherent, fibroblastic, and easy to grow. This makes them ideal candidates for observing interactions with 2D planar materials grown on substrates.

Cells were grown in T25 tissue culture flasks in DMEM with 10% bovine calf serum and 1% penicillin-streptomycin culture media at 37 °C and 5% CO_2. Adhered cells were collected for passaging or counting with 3 mL 0.25% trypsin-EDTA followed washing with Phosphate-buffered saline solution. A hemocytometer (DHC-N01, INCYTO) was used to count cells prior to toxicology experiments. Approximately 2.0 x 10^4 cells were seeded to each material surface and incubated in the culture media.

2.3.b Cell Viability and Toxicity Monitoring

Many studies on the toxicity of 2D materials have focused on determining the cytotoxic effect dependence on its chemical composition, physical and structural characteristics, concentration and duration of time. However, all studies have performed end-point measurements of the cell viability and, therefore, lack information between the introduction of the nanomaterials, and the final measurement step. This work will add a

new set of information by developing a protocol to monitor the cell viability and cytotoxicity of the 2D materials over time, providing useful kinetic information such as the growth and death rate of cells.

In this study, the RealTime-Glo™ MT Cell Viability Assay was used to measure cell viability and CellTox™ Green Cytotoxicity Assay (Promega Corporation) was used for cell cytotoxicity. The mechanism for the cell viability and cytotoxicity kits are shown in Figure 2-9. The viability assay consists of a non-lytic luciferase and a cell-permanent prosubstrate. The prosubstrate enters through the cell and is reduced by the metabolic activity of a living cell. It then exits the cell and reacts with the luciferase enzyme to produce a luminescent signal that is correlated with the number of living cells. The prosubstrate remains unreactive in dead cells and no light is emitted. The cytotoxicity assay involves a cyanine dye that can only enter through the damaged cell membranes of dead cells to bind with the cell's DNA and release a fluorescent signal. This signal is proportional to the number of dead cells. Both assays are able to work in conjunction. Since there is no permanent effect or damage to living cells, the kits can be used to simultaneously and continuously monitor cellular activity for up to 72 hours.

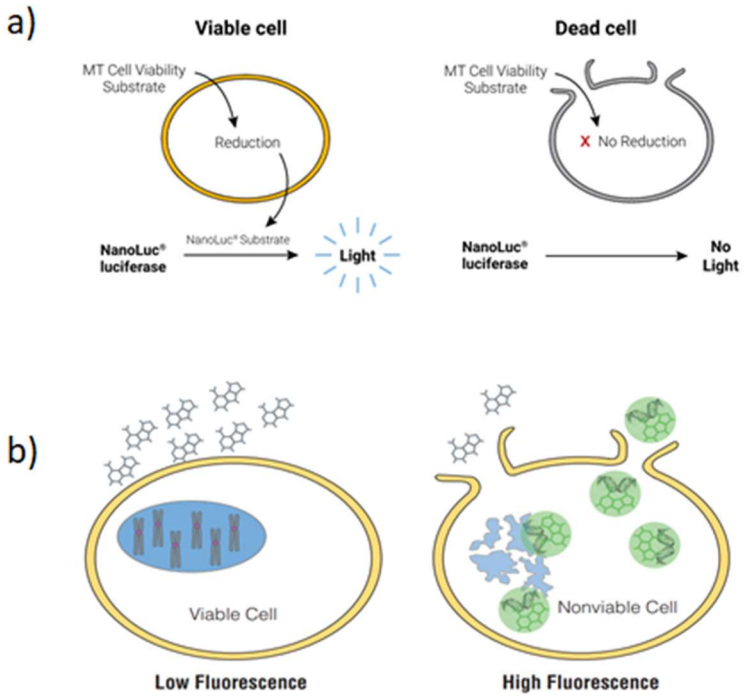

Figure 2-9 a) RealTime-Glo™ MT Cell Viability Assay overview[72] b) CellTox™ Green Cytotoxicity Assay overview[73]

Both luminescence and fluorescence measurements are recorded by a microplate reader. Plate readers consist of a multi-mode spectrometer capable of reading fluorescence, luminescence, and absorbance of the stained cells which is then correlated to cell behavior. The BioTek H1 Plate Reader was used to measure the fluorescence with $485_{emission}/520_{excotatopm}$ and luminescence of the cells in a 96 well plate.

2.3.c Live/Dead Cell Imaging

Live/Dead assays allows for direct imaging of living and dead cells along with their morphology on the substrates through fluorescence microscopy. Fluorescence is analogous to the photoluminescence of crystals mentioned in the earlier section, but this mechanism refers to molecules instead. Invitrogen™ Live/Dead®, viability/cytotoxicity kit for mammalian cells containing calcein AM and ethidium homodimer-1 (EthD-1) was used for fluorescence staining of live and dead cells. The mechanism behind these two

dyes is illustrated in Figure 2-10. The polyanionic calcein AM is a cell-permeable dye that, upon entering living cells, is cleaved by the intracellular esterase enzymes that are characteristic of live cells. Once the AM ester is removed, the membrane-impermanent calcein is permanently retained in the live cell and emits an intense uniform green fluorescence. On the other hand, EthD-1 is a cell impermeable dye that can only enter dead cells with damaged membranes. The dye will then bind with the nuclei, producing a bright red fluorescence at the center of the cell. The dead cells will not interact with calcein AM due to the lack of enzyme activity.

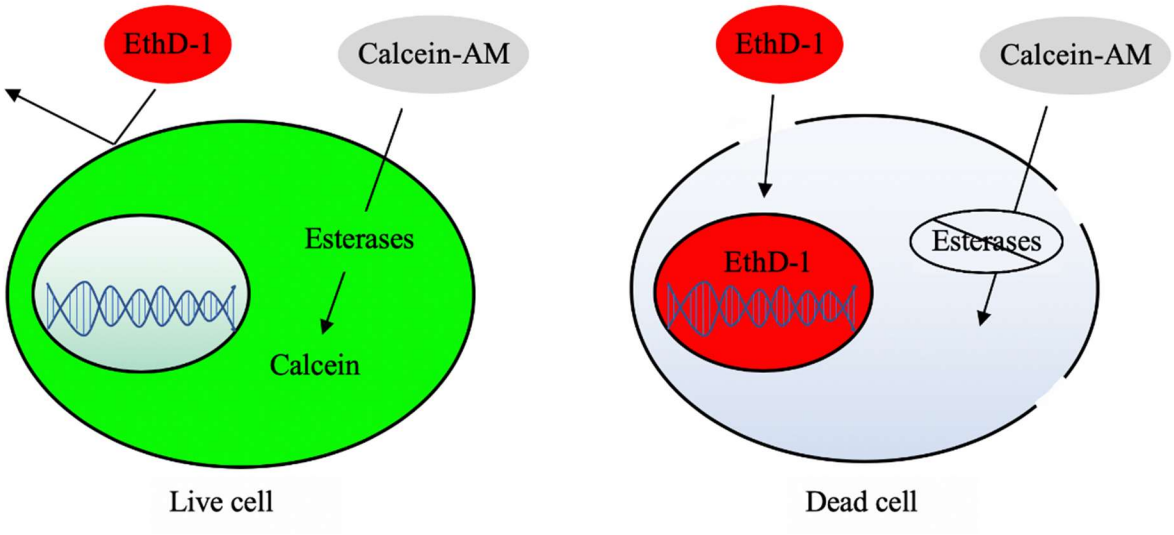

Figure 2-10 Schematic showing staining mechanisms of calcein AM and EthD-1 dyes

An inverted confocal fluorescence microscope was used for the Live/Dead cell imaging and the set-up is shown in Figure 2-11. A laser is used to provide the excitation source. When light hits a sample, the orbital electron is excited and then emits a photon when it relaxes to the ground state. The emitted light is de-scanned from the mirrors and is focused through a pinhole and measured by a photodetector. The pinhole allows for highly effective rejection of out-of-focus fluorescence light and background scatter light

to increase resolution. The entire image can be raster scanned to laterally and with multiple focal planes to provide clean three-dimensional images of the sample.

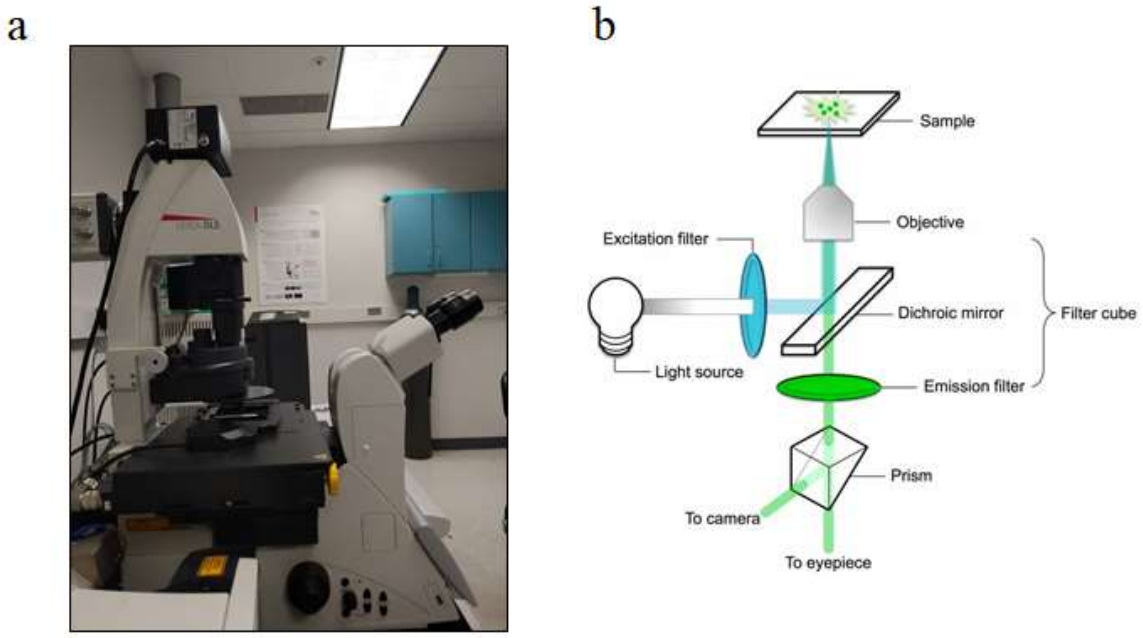

Figure 2-11 a) Fluorescent microscope used to image cells b) Typical schematic of an inverted fluorescent microscope

CHAPTER 3

SYNTHESIS AND CHARACTERIZATION OF TMDCs

3.1 Synthesis of TMDCs

3.1.a Growth of MoS_2

MoS_2 monolayers were grown using the CVD method based on Zande et al.'s set-up and sodium chloride (NaCl) assisted growth based on other literature.[55,58] Figure 3-1a shows the set-up for this particular synthesis. Precursors used were NaCl, molybdenum oxide (MoO_3), and sulfur. Clean sapphire substrates were placed face-down above a ceramic crucible containing 2.3 mg of molybdenum oxide crushed with a small pellet of NaCl crystal. The crucible is loaded into the center of a 1-inch glass tube. The tube was then placed at the central heating zone of the CVD furnace and a secondary crucible filled with melted sulfur was placed approximately 18.5 cm upstream. The growth was done in atmospheric pressure under a constant flow of 23 sccm ultrahigh purity nitrogen (N_2) gas. Samples were first purged with nitrogen gas for 10 minutes at room temperature and another 10 minutes at 300 °C. The temperature is ramped up to 697 °C in 12 minutes and rested there for another 8 minutes. The crystal growth is followed by natural cooling to 650 °C, opening of the furnace hood by an inch until 550 °C, opening of the hood by 2 inches until 450 °C, and finally opening the hood completely for rapid cooling. This process was optimized to produce the largest and cleanest MoS_2 monolayered triangles, optically shown in Figure 3-1b.

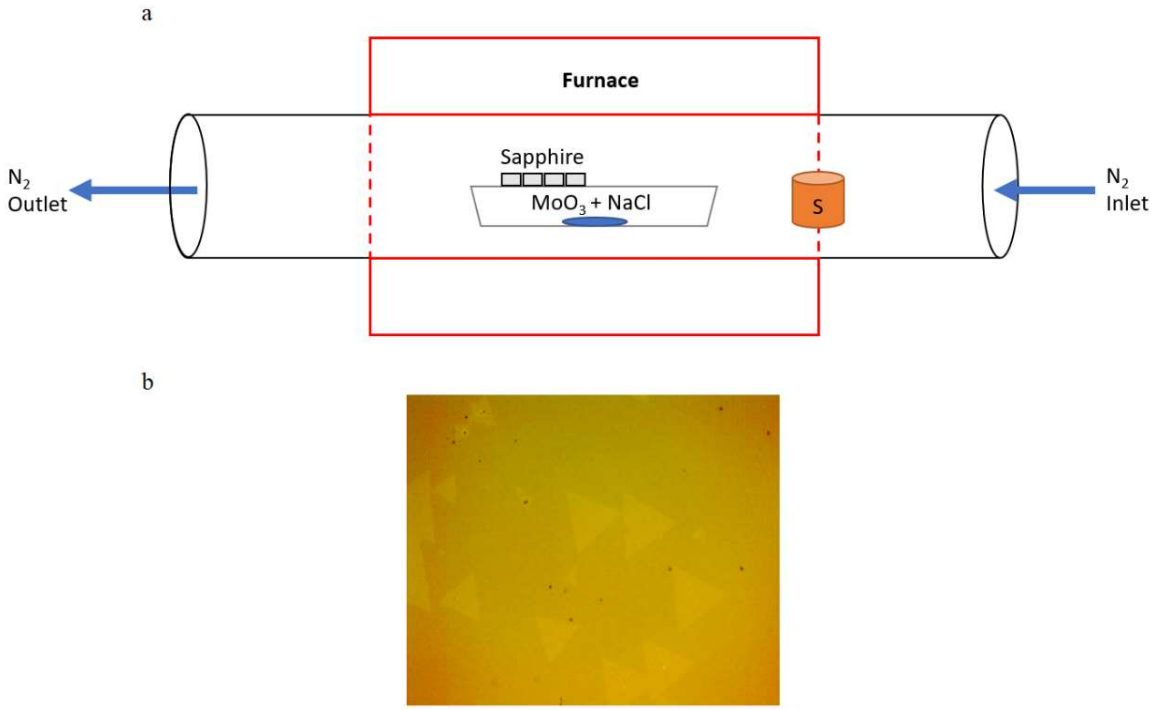

Figure 3-1 a) Schematic of set-up used in CVD of MoS_2 b) Optical image of MoS_2 crystals

3.1.b Exfoliation of MoS_2

Thin MoS_2 flakes were exfoliated from 44 μm powder using a similar method to Bernal et al.[74] A 10mL mixture of 70/30 by volume of IPA/Di water with an initial concentration of 2mg/mL MoS_2 was placed into a glass vial. The beaker was submerged in an ice bath for temperature control and replaced every 30 minutes once the ice melted. MoS_2 nanosheets were obtained by sonication of the bulk MoS_2 at 125 W in ambient environment for 1 hour and 30 minutes with 6s on and 2s off pulse to prevent excessive heating to the sample and reduce evaporation of IPA.

After sonication, the samples were subjected to liquid centrifugation cascade. The samples were transferred to 15 mL tubes and centrifuged at 1000G RCF for 1 hour to remove the bulk unexfoliated MoS2 flakes. The subsequent sediment is discarded, and

the supernatant is exposed to a second centrifugation step at 5500G RCF for 1 hour to further isolate thinner flakes. The sediment and supernatant of each centrifugation is displayed in Figure 3-2. The clear yellow solution is a typical indicator of successful MoS_2 exfoliation into nanosheets. The final solution was evaporated in a vacuum oven to remove the IPA/DI water solution and extract the nanosheets for later toxicity studies.

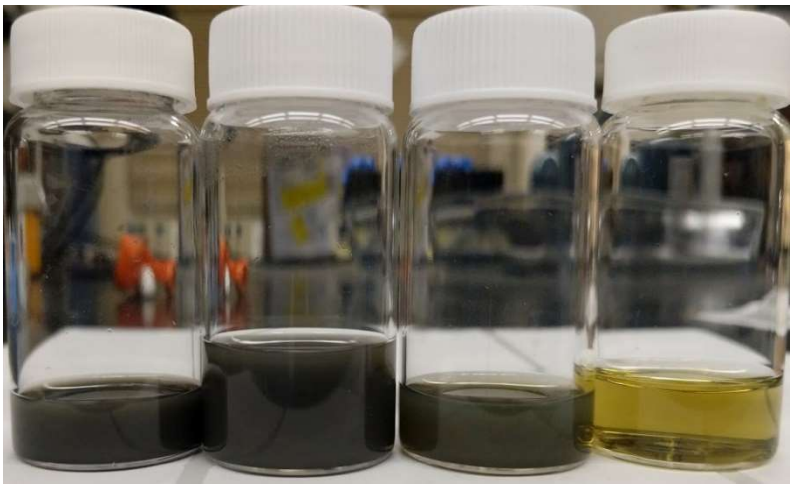

Figure 3-2. From left to right; samples of the freshly exfoliated solution, unexfoliated sediment of the 1st centrifugation step, supernatant of the 1st step, and final supernatant solution

3.1.c Growth of MoSSe

MoSSe Janus monolayers were synthesized from the plasma-assisted surface stripping process, illustrated in Figure 3-3a. CVD grown MoS_2 on sapphire substrates were placed on a quartz boat, positioned 0.9 cm away from end of plasma tail. Re-solidified Se source was placed 6.5 cm upstream away from plasma tail on a second boat. H_2 gas flow rate was set to 30 sccm and the vacuum pump was set to 22 mTorr. The measured pressure of the system was kept constant at 298 mTorr. The RF source was set to 15 W, and the entire process ran for 22 minutes. Optical images of MoSSe flakes are

shown in Figure 3-3a, revealing a large quantity of bulk deposits surrounding and on the triangles. These deposits were further characterized with AFM in a later section.

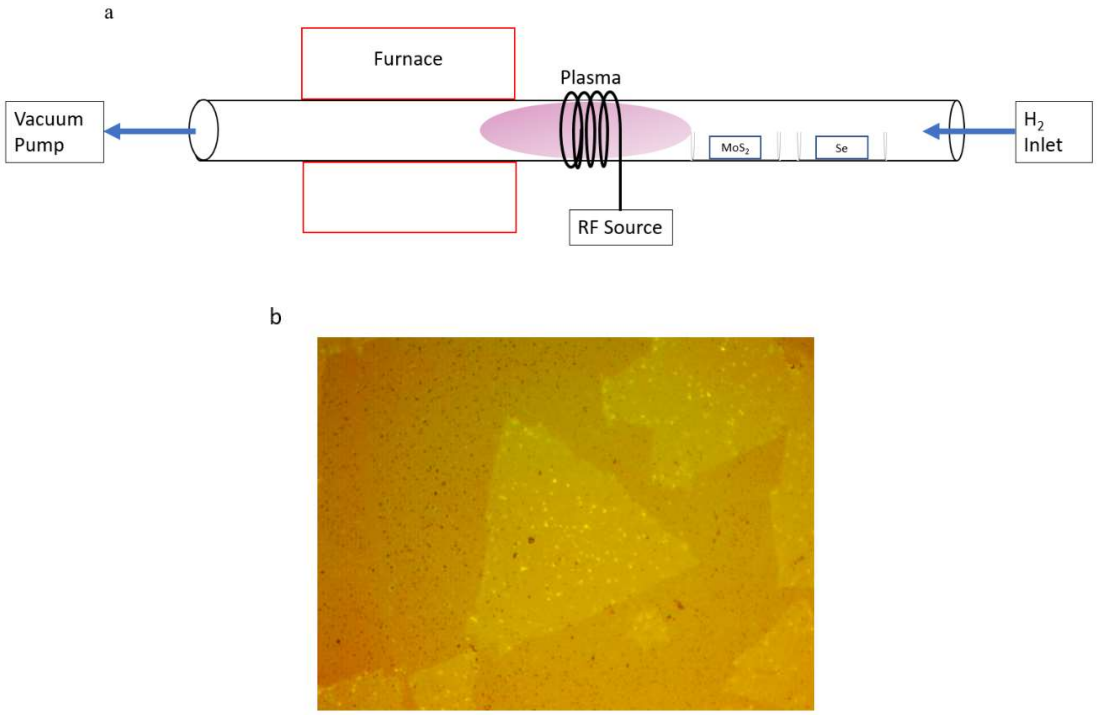

Figure 3-3 a) Schematic of plasma-stripping process of MoS_2 to MoSSe Janus crystals b) Optical images of MoSSe Janus flakes

3.1.d Growth of $MoTe_2$

$MoTe_2$ was synthesized from the MBE process. The setup is shown in Figure 3-4. Mo and Te sputtering targets were used as the precursor. The deposition rate was controlled by the sputtering power, which was set at 15 W for Mo and 450 W for Te targets. The MBE chamber was pumped with argon gas to elevate the pressure to 150 mTorr. This was done to decrease the growth rate and reduce the kinetic energy of the impinging species at the surface to improve the crystallization process. Mo and Te was sputtered at room temperature. After deposition, the substrate temperature was raised to

450 °C and annealed for 2 minutes followed by natural cooling. This process produced an ultra-thin film covering the surface of the sapphire substrate.

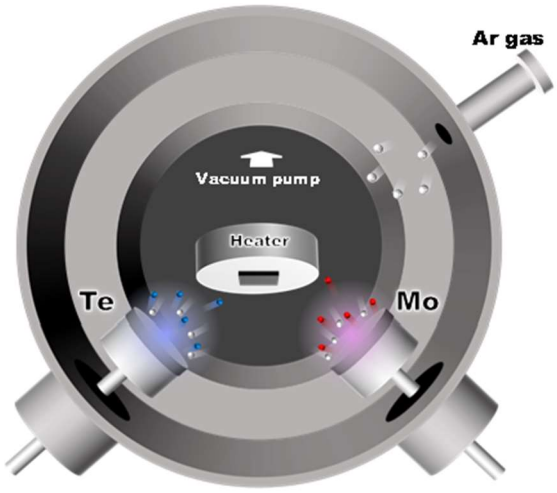

Figure 3-4 Schematic of MBE chamber set-up for epitaxial growth of $MoTe_2$[75]

3.2 Vibrational Studies of TMDCs

3.2.a MoS_2

Bulk MoS_2 has two distinct Raman modes at 383 cm^{-1} (E^1_{2g}) and 408 cm^{-1} (A_{1g}). The E^1_{2g} mode is an in-plane vibrational mode of the two sulfur atoms vibrating opposite to molybdenum atom. The A_{1g} mode is associated with out-of-plane vibrations of the sulfur atoms vibrating in opposite directions to each other. As MoS_2 transitions to a single layer, the two modes evolve with the thickness. The E^1_{2g} mode upshifts to about 386 cm^{-1}, and the A_{1g} mode downshifts to around 404 cm^{-1}. The Raman for CVD grown MoS_2 and bulk MoS_2 powder is compared in Figure 3-5. The spectrum confirms the relative upshift of the E^1_{2g} and downshift of the A_{1g} modes, characteristic of the transition to monolayer thickness.

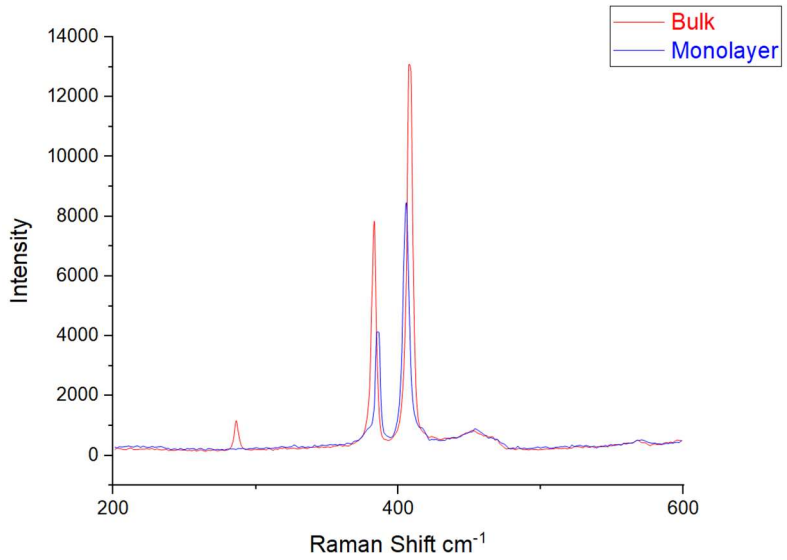

Figure 3-5 Raman spectrum of synthesized MoS_2 and purchased MoS_2 crystals

3.2.b MoSSe

As mentioned earlier, MoS_2 monolayer has the E^1_{2g} mode at 386 cm^{-1} and the A_{1g} mode at 404 cm^{-1}. During the stripping of the top sulfur layer, the intensity of these two vibrational modes will decrease and completely vanish when the sulfur layer is completely removed. After selenization, it is expected that the A_{1g} peak will downshift to about 288 cm^{-1} caused by the out-of-plane symmetry change, and the E^1_{2g} mode will shift to about 355 cm^{-1} due to the change in the lattice constant.

Figure 3-6 shows the Raman spectra for as synthesized MoSSe and MoS_2 for comparison. The relative downshifts of the A_{1g} and E^1_{2g} matches the experimental peaks and predicted phonon calculations in literature, confirming the presence of MoSSe Janus crystals.[32] However, there are still residual MoS_2 peaks, specifically at the A_{1g} vibrational mode. These peaks indicate only partial selenization was done and there are still remaining MoS_2 phases in the monolayers.

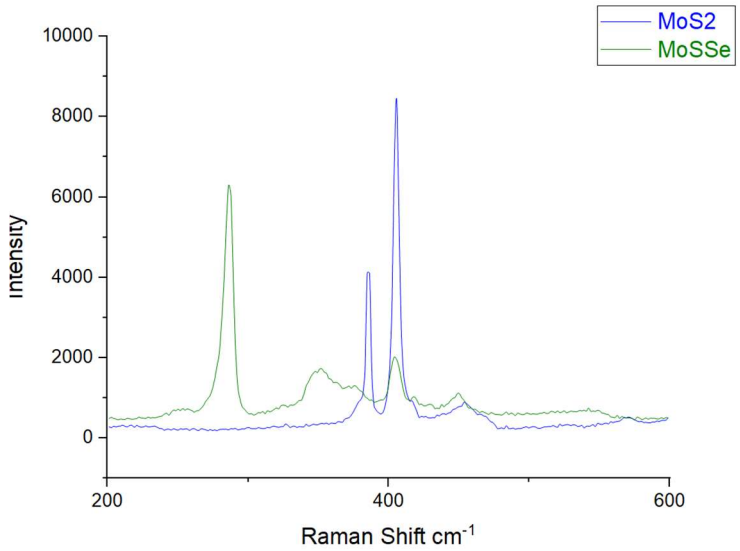

Figure 3-6 Raman spectrum of synthesized MoSSe and MoS_2

3.2.c $MoTe_2$

$MoTe_2$ bulk crystals show two distinct Raman peaks at the out-of-plane A_{1g} mode at 172 cm^{-1} and in-plane E^1_{2g} mode at 233 cm^{-1}.[76] Interestingly, an additional B^1_{2g} mode at 291 cm^{-1} becomes active in the mono- and bi-layer phase due to breaking of the translation symmetry along the c-axis direction. The Raman spectrum of as-grown $MoTe_2$, shown in Figure 3-7, displays a wide peak at around 170 cm^{-1}, characteristic of the A_{1g} mode. However, the other characteristic peaks could not be distinguished. This spectrum suggested that the material is highly defective.

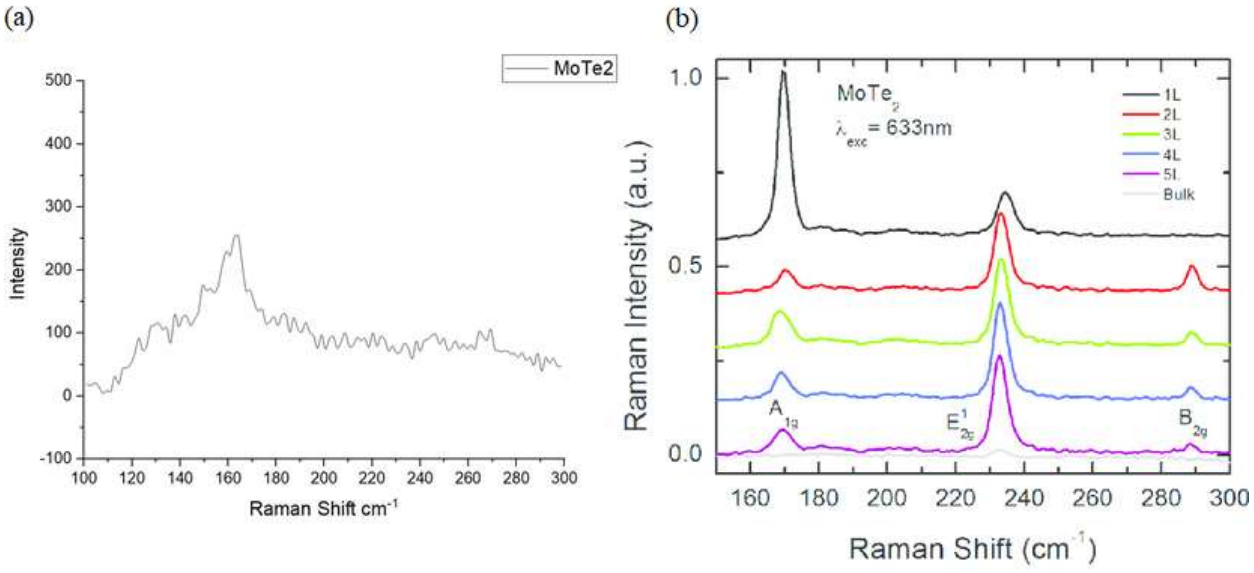

Figure 3-7 a) Raman spectra of synthesized $MoTe_2$ b) Raman spectra of published monolayer, few layers, and bulk $MoTe_2$[77]

3.3 PL Studies of TMDCs

3.3.a MoS_2

As mentioned in the introduction of TMDCs, all MoX_2 materials experience a direct bandgap transition at the single layer thickness, allowing for efficient electron-hole recombination and photoluminescence emission. MoS_2 monolayer produces an intense photoluminescence emission at around 1.8 eV. The PL, shown in Figure 3-8, displays an intense PL signal around 1.83 eV, confirming that the CVD MoS_2 as single layer thickness.

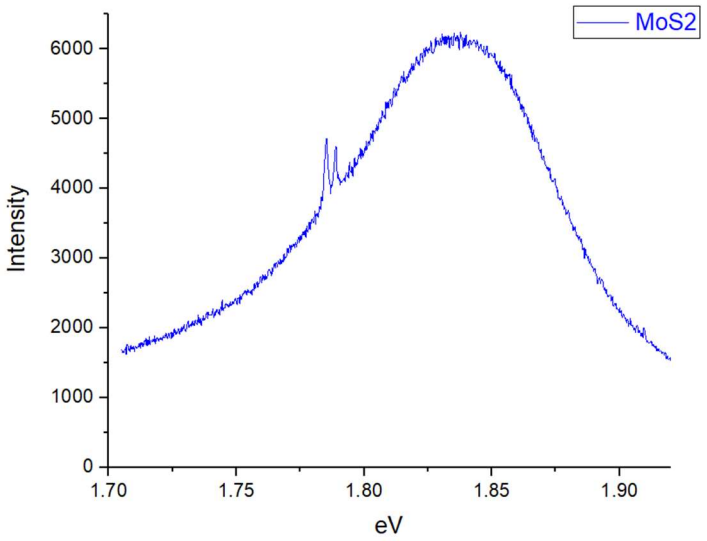

Figure 3-8 PL spectra of synthesized MoS_2

3.3.b MoSSe

According to alloying theory, monolayer MoSSe should have PL peak between the bandgaps of 1.81 eV of MoS_2 and 1.55 eV of $MoSe_2$. The PL spectra of the as synthesized MoS_2 and MoSSe are shown in Figure 3-9 for side-by-side comparison. Compared to literature's value of 1.68 eV, the PL peak of MoSSe here is significantly blue-shifted at 1.73 eV. In conjunction with the previous Raman spectra, the Janus materials synthesized here have properties indicating some leftover MoS_2 phases.

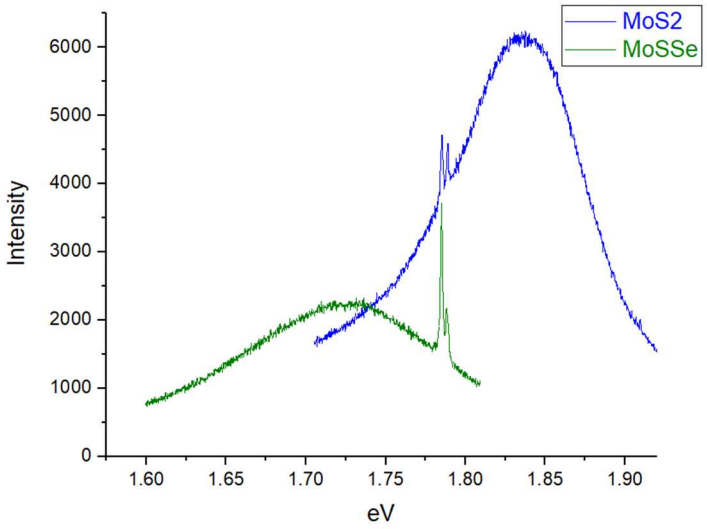

Figure 3-9 PL spectra of synthesized MoSSe and MoS_2

3.3.c $MoTe_2$

$MoTe_2$ is also expected to have a crossover from indirect to direct bandgap at single layer thickness with an optical bandgap of around 1.1 eV. The results from Figure 3-9 show no PL, confirming that the grown $MoTe_2$ is highly defective and greater than atomic level thickness.

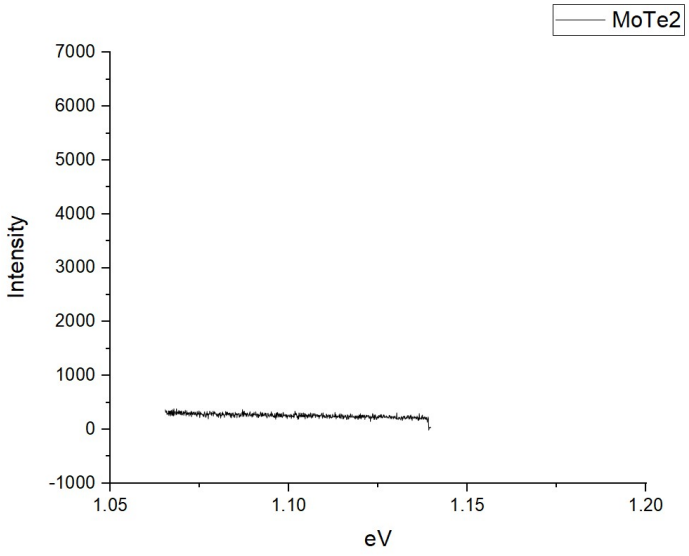

Figure 3-10 PL spectra of synthesized $MoTe_2$

3.4 Morphology and Thickness Characterization of TMDCs

3.4.a MoS_2

Monolayer MoS_2 has an atomic thickness of around 0.6 nm. However, growth on different substrates can lead to variable thickness measurements for monolayers. In Figure 3-10, an AFM image and height profile of a MoS_2 crystal is shown. The image shows a clean MoS_2 flake. Height profile shows roughly 0.8 nm thickness, which correlates to a single atomic layer on sapphire. The topography images and characterization spectrums together suggest highly crystalline monolayers were synthesized.

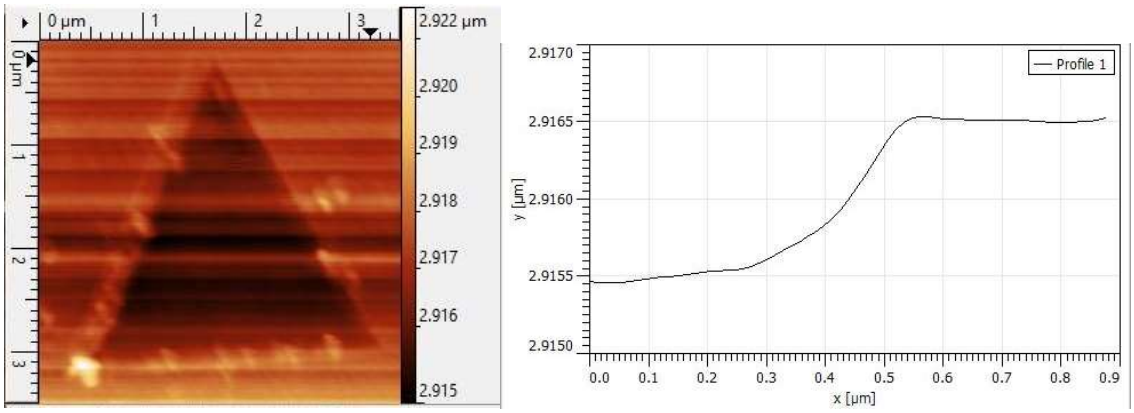

Figure 3-11 AFM topography (left) and height profile (right) of MoS_2 flake

The morphology and thickness of the MoS_2 nanosheets is shown in Figure 3-11. To prepare the suspended flakes for AFM measurements, 10µL of the final supernatant solution was dispensed onto a heated SiO_2 substrate to quickly evaporate the solution. The sample is then gently washed with DI water to remove organic residue. There are polydisperse nanosheets with thicknesses ranging from 1nm to 50 nm.

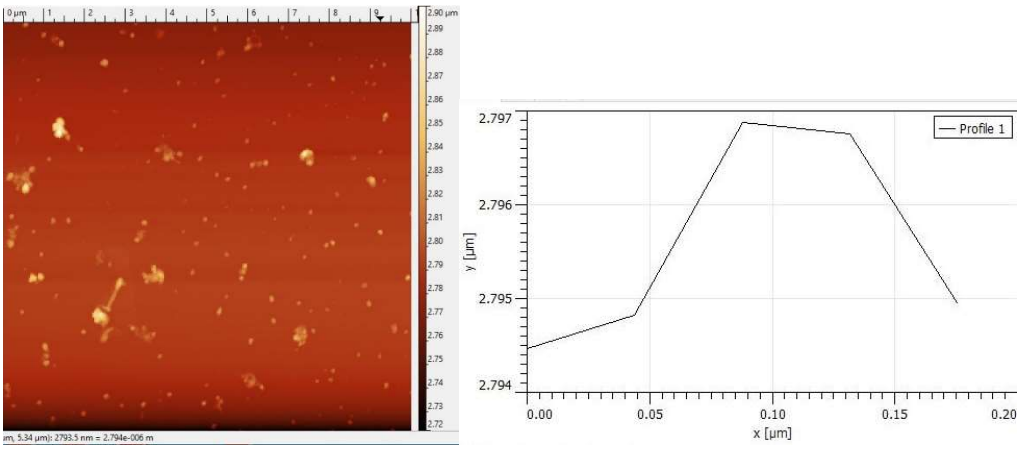

Figure 3-12 AFM topography (left) and height profile (right) of LPE MoS_2 flakes

3.4.b MoSSe

MoSSe monolayers are also expected to have monolayer thickness of around 0.6 nm. The image shown in Figure 3-12 shows single atomic thickness of 0.77 nm. After the stripping and selenization process, the topography shows a large quantity of selenium deposits. Additionally, the topography images show defects along the edges of the monolayer triangles.

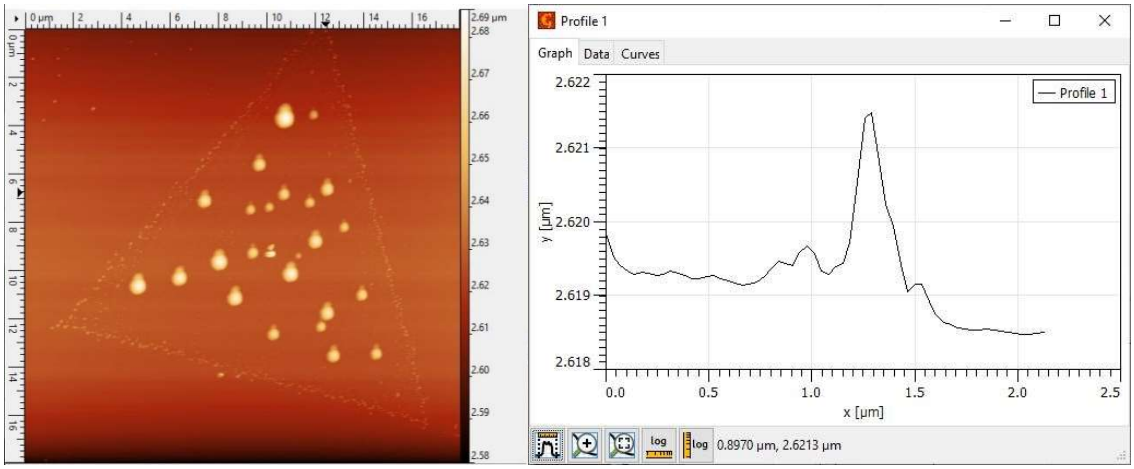

Figure 3-13 AFM topography (left) and profile height (right) of MoSSe flake

3.4.c $MoTe_2$

A single layer of $MoTe_2$ has an estimated atomic thickness of 0.7 nm. The AFM image in Figure 3-13 shows a bulk layered material with large number of discontinuous grains and vacancies. The height profile showed an average thickness of around 12-14 nm corresponding to about 20 layers. Coupled with the poor Raman signals, this indicates a highly defective thin film was synthesized.

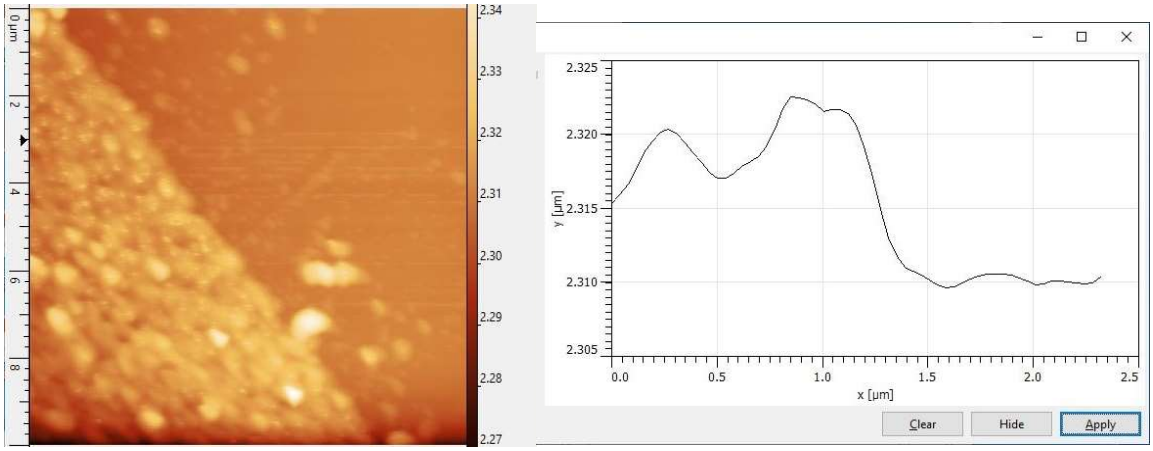

Figure 3-14 AFM topography (left) and profile height (right) of $MoTe_2$ thin film

CHAPTER 4

TOXICOLOGY OF TMDCs

4.1 Cell Viability and Toxicity Monitoring of TMDCs

4.1.a Sample Preparation

Four subsections of bare sapphire, CVD MoS_2, $MoSe_2$, and MoSSe, MBE $MoTe_2$, and LPE MoS_2 samples were placed into a 96-well plate, with the substrates covering 50% of the available well growth area. 100 μL of culture media with 2 x 10^3 cells were seeded into each well and incubated at 37 °C in a 5% CO_2 environment for 56 hours. Both the RealTime-Glo™ assay for measuring cell viability and CellTox™ assay for measuring cytotoxicity were added at the seeding of the cells at 1X dilutions according to manufacturing instructions. The luminescent and fluorescence was then recorded manually by the plate reader every 4 hours.

4.1.b Cell Viability

The seeded cells will start to adhere onto the substrates within an hour and interaction effects with the 2D materials can be observed from this point in time. Healthy cells are expected to grow at an approximately linear rate, doubling their cell quantity every 20-26 hours. A plot of the cell proliferation rate of all samples are shown in Figure 4-1. Saturation of the proliferation rate was observed after 40 hours; however, this will occur when the cell line has reached the maximum reducing capacity of the MT Cell Viability substrate. CVD MoS_2 and MoSSe exhibited similar proliferation rates and linear cell growth in comparison with the control sapphire adhered cells. $MoTe_2$ and LPE MoS_2 showed a decreasingly lower luminescence signal than the other three materials. After 40 hours, these two materials displayed less than half the luminescence of the clean sapphire

substrate luminescence signal, correlating to approximately less than half the number of living cells as sapphire adhered cells.

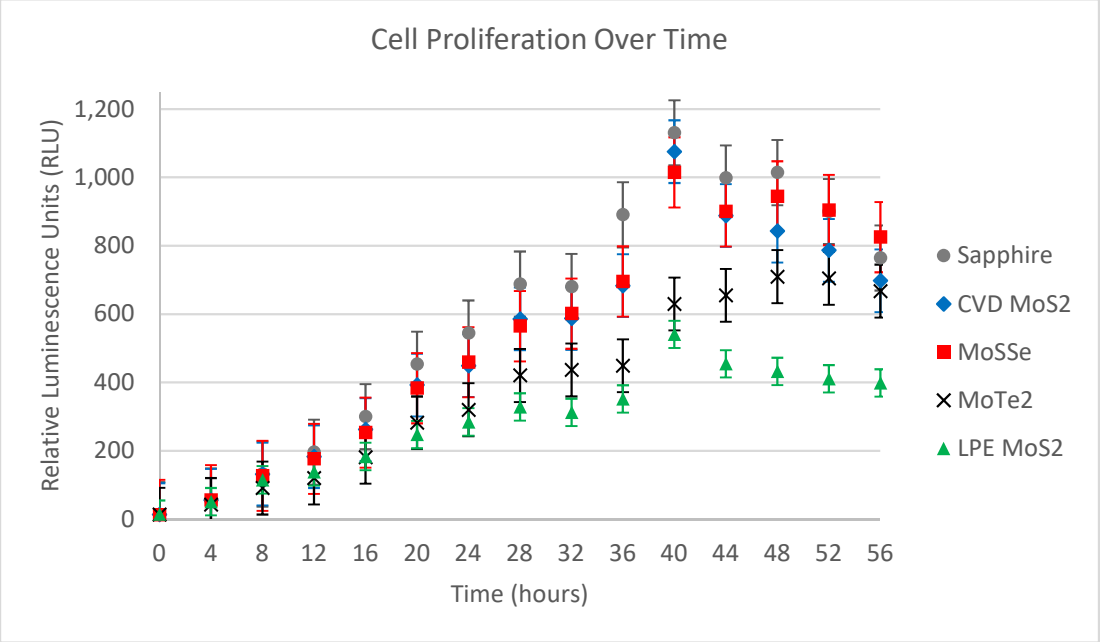

Figure 4-1 Cell viability monitoring of samples with RealTime-Glo™ assay

A closer look at the cell proliferation from 0 to 16 hours is shown in Figure 4-2. The growth for all materials follows a linear rate up until the 8-hour mark. After 8 hours, LPE MoS_2 and $MoTe_2$ started to exhibit reduced growth. Every measurement thereafter, the luminescence intensity further deviates from the sapphire, MoSSe, and CVD MoS_2 linear growth rate. This trend suggests that the cellular growth rate for these two materials were slowing down as time progresses.

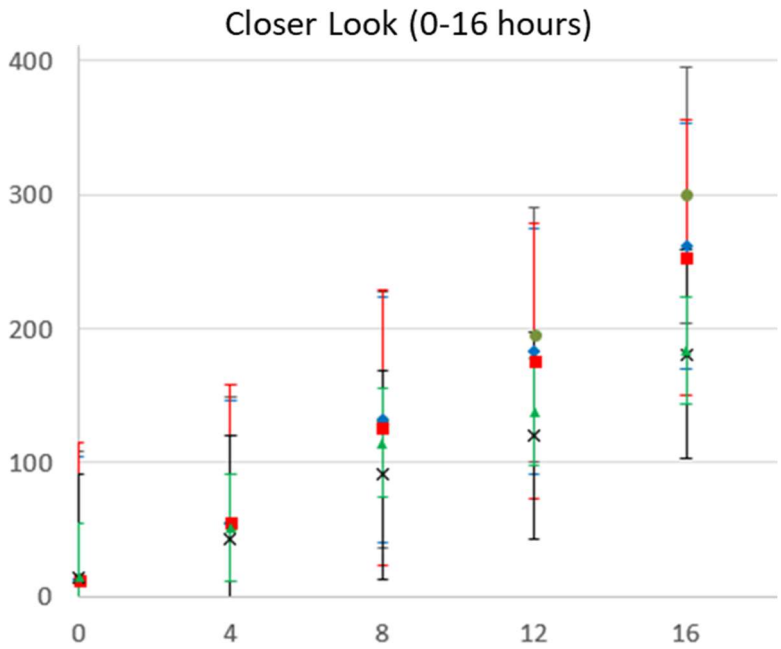

Figure 4-2 A closer at 0-16 hour time period of Figure 4-1

4.1.c Cytotoxicity

The fluorescence signal of cells should remain constant until there is an increase in cellular death. Figure 4-3 shows the monitoring of cellular death with large fluctuations in the fluorescence signals by hour for all materials with no general trends. The results from this graph shows inconclusive data.

An additional study was done with two control groups of untreated cells and lysed cells to further understand the results from the CellTox™ assay, shown in Figure 4-4. The lysed cells, representing 100% dead cells, showed an intense fluorescence signal of around 5 x 10^4 RFU. The untreated cells and the 2D material's fluorescence signals were found to be statistically similar, slightly below 1 x 10^3 RFU. These results suggest the cell cytotoxicity measurements were within the sensitivity of the technique, and not enough cells were killed by the 2D materials to the plate reader to detect a significant

signal. This also supports the conclusion that cells are not dying, but instead are experience inhibited growth rates.

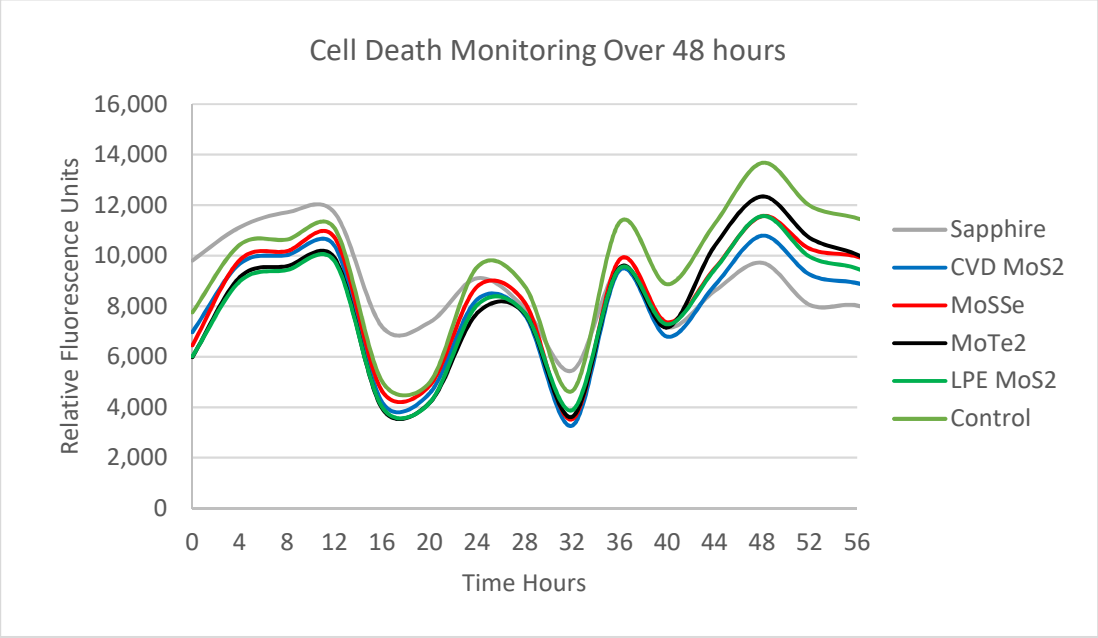

Figure 4-3 Cell death monitoring of samples with CellTox™ assay

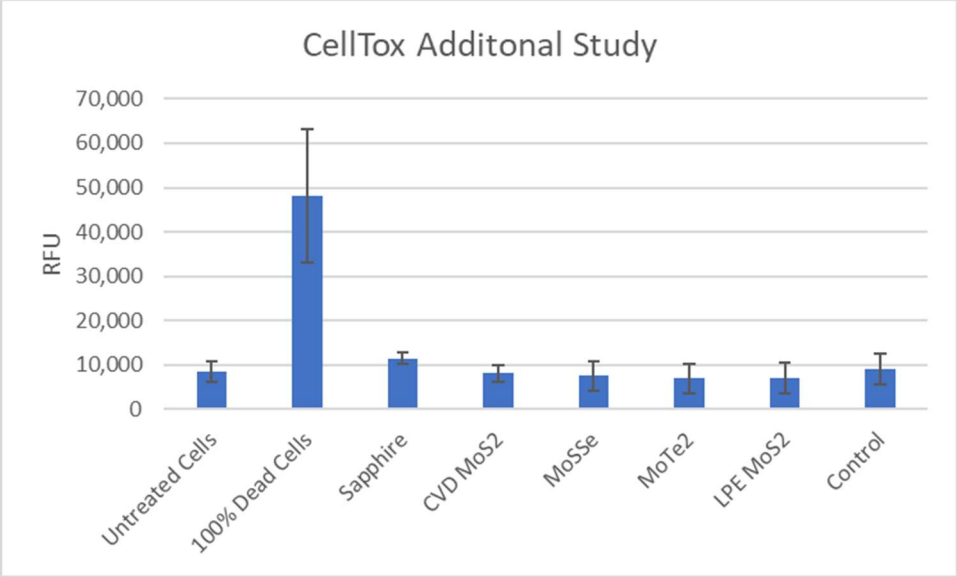

Figure 4-4 Additional study done with CellTox™ measuring fluorescence of untreated cells and completely dead cell control groups.

4.2 Live/Dead Imaging of TMDCs

4.2.a Sample Preparation Procedure

Four subsections of MoS_2, and MoSSe, $MoTe_2$, and MoS_2 samples each were placed face-up into a 24-well plate. The 400 µL of culture media was dispensed into each well with a seeding density of 5.0 x 10^4 cells. For the LPE MoS_2, 200 µL of 5.0 x 10^4 cells were seeded onto 4 subsections of sapphire substrates. An additional 200 µL of cell media dispersed with 100 µg/mL Lpe MoS_2. After 48 hours, the samples were incubated for 30 minutes in a PBS solution containing 2 µM calcein AM and 4 µM EthD-1 at 37 °C and 5% CO_2. The samples were then individually imaged under the inverted fluorescent confocal microscope. The images were done in a raster scan over 1 mm^2 surface of the substrates.

4.2.b Sapphire

After 48 hours of incubation, cells grown on sapphire show high cell viability based on optical observation. Images such as Figure 4-5 show strong and healthy cells forming dense fibrous networks typical of NIH 3T3 mouse fibroblasts with no presence of dead cells showing red fluorescence. Utilizing ImageJ software, the confluency of the live cells was approximately 70 ± 3%.

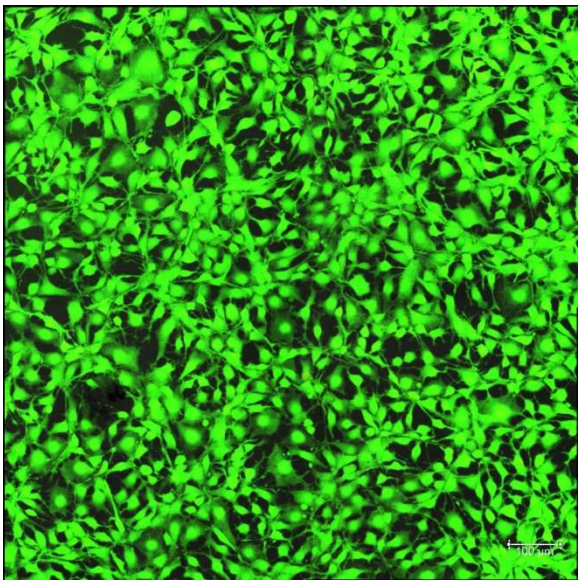

Figure 4-5 Live/dead cell imaging of cells on bare sapphire substrate

4.2.c MoS_2

Figure 4-6 shows the Live/Dead imaging of cells on CVD grown MoS_2. Cell confluency was measured to be approximately 40 ± 4%. After 48 hours of incubation, cells grown on CVD MoS_2 show healthy cell growth based on the fluorescence imaging. Although cell proliferation studies show CVD MoS_2 growth rates to be comparable to sapphire, the quantity of cells observed on the MoS_2 surfaces is significantly lower. This suggests that cellular growth on the MoS_2 surfaces was slowed compared to on clean sapphire substrates. However, since the none of the cells on the substrate are dying, the overall cell proliferation of the well is still high. This agrees well with past studies concluding the high biocompatibility of CVD grown MoS_2 monolayers.[53,56]

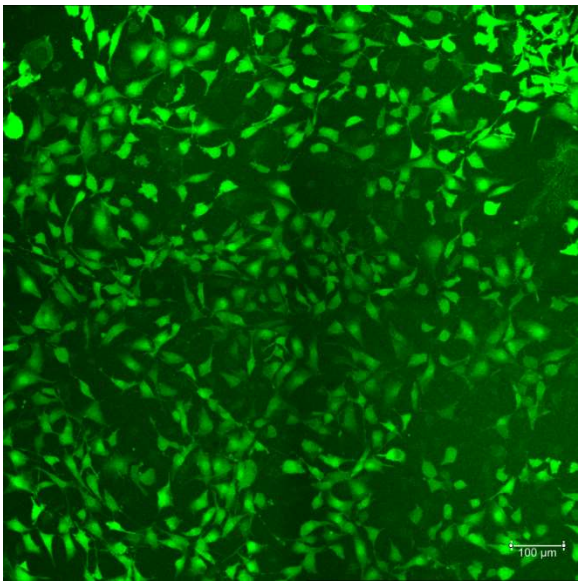

Figure 4-6 Live/Dead cell imaging of cells on CVD MoS_2 substrate

Figure 4-7 shows the Live/Dead image of the cells with several notable dead cells as red dots. Cells cultured on sapphire substrates with LPE MoS_2 suspended flakes showed very low confluency, approximately 29 ± 6%. In addition, there was significant number of red nuclei representing dead cells. A closer look at the morphology shows the cells shrinking and lacking a healthy fibrous network. This suggests the cell are not healthy and under stress due to the presence of the exfoliated sheets. Liquid exfoliated MoS_2's decreased biocompatibility can be attributed to its smaller dimensions, highly defected structure, and increased effective surface area for adverse cellular interactions. Several publications have also commented on the size-dependent toxicity of liquid phase exfoliated MoS_2.[54,78]

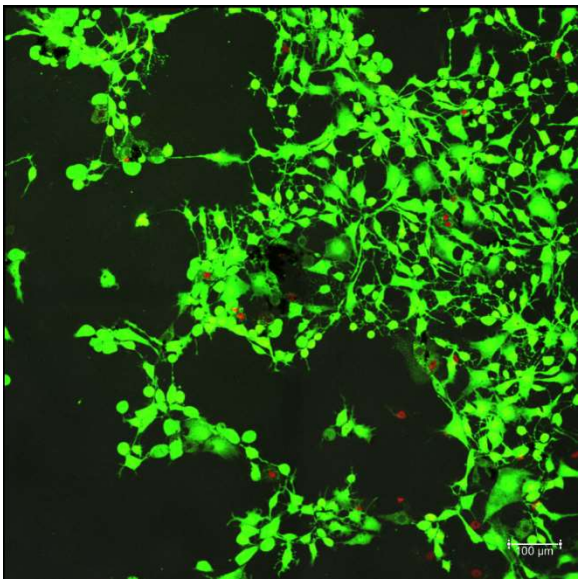

Figure 4-7 Live/Dead cell imaging of cells on LPE MoS_2 substrate

4.2.d MoSSe

After 48 hours of incubation, cells grown on sapphire MoSSe show only living cells with no red dead cells, illustrated in Figure 4-8. Images show strong and healthy cells forming fibrous networks typical of mouse fibroblasts with a cell confluency of 36 ± 5%. MoSSe showed slightly less confluency on its surface than CVD MoS_2 samples. This agrees well with the cell proliferation study since CVD MoS_2's final cell count after 40 hours was slightly higher. Literature has reported the lower cell viabilities of Se TMDCs through studies of chemically exfoliated WS_2, WSe_2, VS_2, and VSe_2, possibly due to the lower stability of Se bonds.[50,52] However, these studies found MoSSe to show similar cell proliferation to MoS_2, suggesting that the sulfur bond plays a role in either stabilizing the Se bonds of Janus crystal and increase the biocompatibility.

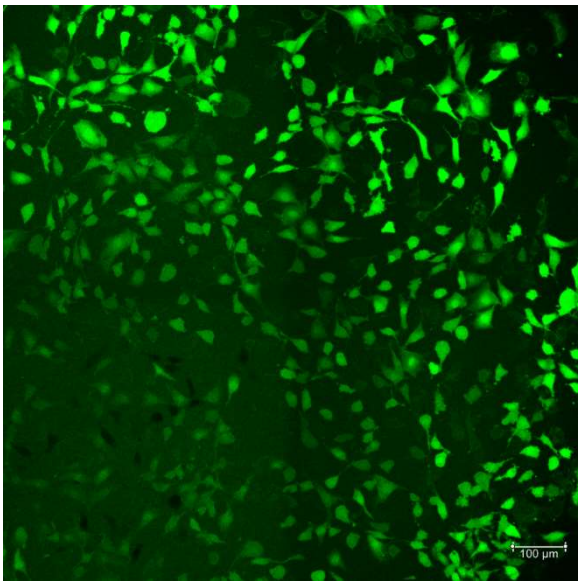

Figure 4-8 Live/Dead cell imaging of cells on MoSSe substrate

4.2.e $MoTe_2$

After 40 hours of incubation, Figure 4-9 shows a significantly lower population density of living cells, without any presence of dead cells grown on the $MoTe_2$ film. Image J measured a low cell confluency of about 25% and the cell viability study also showed low cell proliferation when cells were cultured on $MoTe_2$. Although no dead cells were observed, the low confluency and cell population density suggests unpreferable growth environments for the cells. Tellurium TMDCs has been reported to be generally more toxic than their sulfide counterparts.[51] The highly defective structure of the thin film also could have played an important role in minimizing the cellular adhesion and growth onto the thin films.

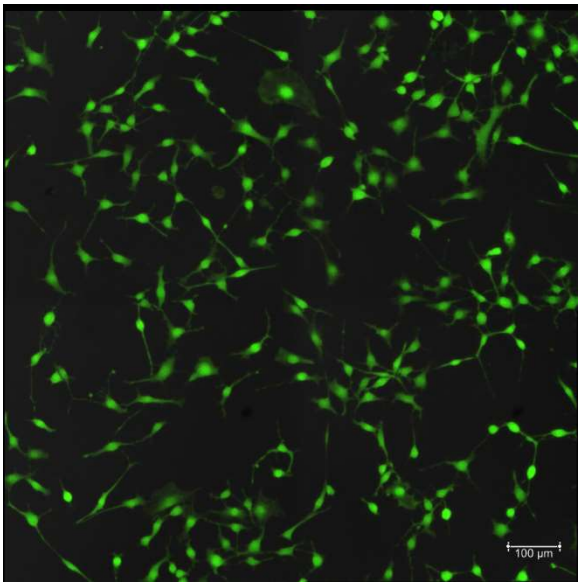

Figure 4-9 Live/Dead cell imaging of cells on MBE $MoTe_2$ substrate

4.3 Summary of Toxicology Studies

Results show the statistically comparable cell proliferation of CVD grown MoS_2 monolayers and MoSSe Janus monolayers to sapphire substrates. However, Live/Dead imaging reveals reduced cell confluency and growth for these 2D materials compared to sapphire. This data suggests that crystalline MoS_2 and MoSSe do not promote cellular growth as well as clean sapphire surfaces. However, these 2D materials do not show any explicitly toxic effects to the cells.

$MoTe_2$ surfaces have also shown reduced cell proliferation as well as confluency. The highly defective structure and telluride chalcogen may have promoted an unfavorable surface for cellular growth. Liquid phase exfoliated MoS_2 sheets in this study have actively killed living cells while inhibiting the cellular growth and health on sapphire substrates, shown in the Live/Dead images.

CHAPTER 5

CONCLUSION AND OUTLOOK

5.1 Conclusion

In this work, a new approach in studying the interactions between 2D materials and biomolecules through kinetic monitoring of the cell proliferation and death was explored. Previous work has focused on end-point measurements after 24- or 48-hour time periods under the assumption that lowered cell viabilities observed by 2D materials were due to the death of cells.

This study has shown that the 2D planar materials MoS_2, MoSSe, and $MoTe_2$ thin films inhibit cell growth but are not directly killing them within the 48-hour period. Highly defective $MoTe_2$ thin films showed significantly reduced cell growth and population density. MoS_2 nanosheets of less than 50 nm sizes have shown reduced cell proliferation as well as a cytotoxic effect, which may be due to an increase in surface area and defects or its small particle size to allow for cellular endocytosis. Overall, these results suggest the increased role defects may have in 2D material biocompatibility.

5.2 Future Directions

The unique properties of 2D materials can unlock exciting applications in quantum information technology and biosensing. The increased interest and potential of these materials demand fundamental understanding of their interactions with environmental and biosystems. Studies like this and others have shown defects in 2D materials play some role in their biocompatibility. Chen et al. demonstrated that the grain boundaries (defects) of MoS_2 monolayer flakes initiated dissociation of the material and increasing the density of grain boundaries increased the dissolution rate.[56] Further studies

on defective 2D planar materials are necessary to determine whether the dissolution rate and the type of defects have a significant impact on the toxicity.

In addition to cytotoxicity and proliferation studies, significant research must be poured into other aspects of material biocompatibility such as biodistribution tests, irritation tests, genotoxicity assays, carcinogenic assays, and much more. The in-depth understanding of 2D material biocompatibility will allow for preventative health and environmental risk assessment as well as furthering development for bio-applications.

REFERENCES

1. Briggs, N. *et al.* A roadmap for electronic grade 2D materials. *2D Materials* **6**, (2019).

2. Novoselov, K. S. *et al.* Electric field in atomically thin carbon films. *Science (80-.).* **306**, 666–669 (2004).

3. Mounet, N. *et al.* Two-dimensional materials from high-throughput computational exfoliation of experimentally known compounds. *Nat. Nanotechnol.* **13**, 246–252 (2018).

4. Molle, A. *et al.* Silicene, silicene derivatives, and their device applications. *Chemical Society Reviews* **47**, 6370–6387 (2018).

5. Liu, H. *et al.* Phosphorene: An unexplored 2D semiconductor with a high hole mobility. *ACS Nano* **8**, 4033–4041 (2014).

6. Zhang, K., Feng, Y., Wang, F., Yang, Z. & Wang, J. Two dimensional hexagonal boron nitride (2D-hBN): synthesis, properties and applications. *J. Mater. Chem. C* **5**, 11992–12022 (2017).

7. Liu, N. *et al.* Recent Progress on Germanene and Functionalized Germanene: Preparation, Characterizations, Applications, and Challenges. *Small* **15**, e1805147 (2019).

8. Choi, W. *et al.* Recent development of two-dimensional transition metal dichalcogenides and their applications. *Mater. Today* **20**, 116–130 (2017).

9. Chen, Y. *et al.* 2D Ruddlesden-Popper Perovskites for Optoelectronics. *Adv. Mater.* **30**, 1703487 (2018).

10. Servalli, M. & Schlüter, A. D. Synthetic Two-Dimensional Polymers. *Annu. Rev. Mater. Res.* **47**, 361–389 (2017).

11. Shams, S. S., Zhang, R. & Zhu, J. Graphene synthesis: A Review. *Materials Science- Poland* **33**, 566–578 (2015).

12. Zhen, Z. & Zhu, H. Structure and Properties of Graphene. in *Graphene* 1–12 (Elsevier, 2018). doi:10.1016/b978-0-12-812651-6.00001-x

13. Papageorgiou, D. G., Kinloch, I. A. & Young, R. J. Mechanical properties of graphene and graphene-based nanocomposites. *Progress in Materials Science* **90**, 75–127 (2017).

14. Pang, S., Hernandez, Y., Feng, X. & Müllen, K. Graphene as transparent electrode material for organic electronics. *Adv. Mater.* **23**, 2779–2795 (2011).

15. Reddy, D., Register, L. F., Carpenter, G. D. & Banerjee, S. K. Graphene field-effect transistors. *J. Phys. D. Appl. Phys.* **44**, 313001 (2011).

16. Xu, C. *et al.* Graphene-based electrodes for electrochemical energy storage. *Energy and Environmental Science* **6**, 1388–1414 (2013).

17. Shao, Y. *et al.* Graphene based electrochemical sensors and biosensors: A review. *Electroanalysis* **22**, 1027–1036 (2010).

18. Jiang, Y., Biswas, P. & Fortner, J. D. A review of recent developments in graphene-enabled membranes for water treatment. *Environ. Sci. Water Res. Technol.* **2**, 915–922 (2016).

19. Guinea, F., Katsnelson, M. I. & Geim, A. K. Energy gaps and a zero-field quantum hall effect in graphene by strain engineering. *Nat. Phys.* **6**, 30–33 (2010).

20. Cheng, S. H. *et al.* Reversible fluorination of graphene: Evidence of a two-dimensional wide bandgap semiconductor. *Phys. Rev. B - Condens. Matter Mater. Phys.* **81**, (2010).

21. Hicks, J. *et al.* A wide-bandgap metal-semiconductor-metal nanostructure made entirely from graphene. *Nat. Phys.* **9**, 49–54 (2013).

22. Duan, X., Wang, C., Pan, A., Yu, R. & Duan, X. Two-dimensional transition metal dichalcogenides as atomically thin semiconductors: Opportunities and challenges. *Chem. Soc. Rev.* **44**, 8859–8876 (2015).

23. Podzorov, V., Gershenson, M. E., Kloc, C., Zeis, R. & Bucher, E. High-mobility field-effect transistors based on transition metal dichalcogenides. *Appl. Phys. Lett.* **84**, 3301–3303 (2004).

24. Wang, J., Verzhbitskiy, I. & Eda, G. Electroluminescent Devices Based on 2D Semiconducting Transition Metal Dichalcogenides. *Advanced Materials* **30**, (2018).

25. Li, B. L. *et al.* Low-Dimensional Transition Metal Dichalcogenide Nanostructures Based Sensors. *Adv. Funct. Mater.* **26**, 7034–7056 (2016).

26. Pumera, M., Sofer, Z. & Ambrosi, A. Layered transition metal dichalcogenides for electrochemical energy generation and storage. *J. Mater. Chem. A* **2**, 8981–8987 (2014).

27. Huo, N., Yang, Y. & Li, J. Optoelectronics based on 2D TMDs and heterostructures. *J. Semicond.* **38**, (2017).

28. Maniadaki, A. E., Kopidakis, G. & Remediakis, I. N. Strain engineering of electronic properties of transition metal dichalcogenide monolayers. *Solid State*

Commun. **227**, 33–39 (2016).

29. Lin, Z., Mccreary, A. & Briggs, N. Defect engineering of two-dimensional transition metal dichalcogenides. (2016). doi:10.1088/2053-1583/3/2/022002

30. Komsa, H. P. *et al.* Two-dimensional transition metal dichalcogenides under electron irradiation: Defect production and doping. *Phys. Rev. Lett.* **109**, (2012).

31. Kutana, A., Penev, E. S. & Yakobson, B. I. Engineering electronic properties of layered transition-metal dichalcogenide compounds through alloying. *Nanoscale* **6**, 5820–5825 (2014).

32. Lu, A. Y. *et al.* Janus monolayers of transition metal dichalcogenides. *Nat. Nanotechnol.* **12**, 744–749 (2017).

33. Li, R., Cheng, Y. & Huang, W. Recent Progress of Janus 2D Transition Metal Chalcogenides : From Theory to Experiments. **1802091**, 1–11 (2018).

34. Mak, K. F., Lee, C., Hone, J., Shan, J. & Heinz, T. F. Atomically thin MoS2: A new direct-gap semiconductor. *Phys. Rev. Lett.* **105**, 2–5 (2010).

35. Zeng, H., Dai, J., Yao, W., Xiao, D. & Cui, X. Valley polarization in MoS 2 monolayers by optical pumping. *Nat. Nanotechnol.* **7**, 490–493 (2012).

36. Splendiani, A. *et al.* Emerging photoluminescence in monolayer MoS 2. *Nano Lett.* **10**, 1271–1275 (2010).

37. Tongay, S. *et al.* Thermally driven crossover from indirect toward direct bandgap in 2D Semiconductors: MoSe2 versus MoS2. *Nano Lett.* **12**, 5576–5580 (2012).

38. Ruppert, C., Aslan, O. B. & Heinz, T. F. Optical properties and band gap of single- and few-layer MoTe2 crystals. *Nano Lett.* **14**, 6231–6236 (2014).

39. Manzeli, S., Ovchinnikov, D., Pasquier, D., Yazyev, O. V. & Kis, A. 2D transition metal dichalcogenides. *Nat. Rev. Mater.* **2**, 17033 (2017).

40. Cheng, Y. C., Zhu, Z. Y., Tahir, M. & Schwingenschlögl, U. Spin-orbit-induced spin splittings in polar transition metal dichalcogenide monolayers. *EPL* **102**, (2013).

41. Cui, C., Xue, F., Li, L. J. & Hu, W. J. Erratum to: Two-dimensional materials with piezoelectric and ferroelectric functionalities (npj 2D Materials and Applications, (2018), 2, 1, (18), 10.1038/s41699-018-0063-5). *npj 2D Mater. Appl.* **2**, (2018).

42. Tan, X., Smith, S. C. & Dai, Y. A Janus MoSSe monolayer : a superior and. 1099–1106 (2019). doi:10.1039/c8ta08407f

43. Zhang, J. *et al.* Janus Monolayer Transition-Metal Dichalcogenides. *ACS Nano* **11**, 8192–8198 (2017).

44. Ma, X., Yong, X., Jian, C. & Zhang, J. Transition Metal-Functionalized Janus MoSSe Monolayer: A Magnetic and Efficient Single-Atom Photocatalyst for Water-Splitting Applications. *J. Phys. Chem. C* **123**, 18347–18354 (2019).

45. Choi, W. *et al.* Recent development of two-dimensional transition metal dichalcogenides and their applications. *Materials Today* **20**, 116–130 (2017).

46. Merlo, A., Mokkapati, V. R. S. S., Pandit, S. & Mijakovic, I. Boron nitride nanomaterials: Biocompatibility and bio-applications. *Biomater. Sci.* **6**, 2298–2311 (2018).

47. Nath, N. C. D., Debnath, T., Nurunnabi, M. & Kim, E.-K. *In Vitro Toxicity of 2D Materials*. *Biomedical Applications of Graphene and 2D Nanomaterials* **2004**, (Elsevier Inc., 2019).

48. Kenry & Lim, C. T. Biocompatibility and nanotoxicity of layered two-dimensional nanomaterials. *ChemNanoMat* **3**, 5–16 (2017).

49. Guiney, L. M., Wang, X., Xia, T., Nel, A. E. & Hersam, M. C. Assessing and Mitigating the Hazard Potential of Two-Dimensional Materials. *ACS Nano* **12**, 6360–6377 (2018).

50. Teo, W. Z., Chng, E. L. K., Sofer, Z. & Pumera, M. Cytotoxicity of exfoliated transition-metal dichalcogenides (MoS 2, WS2, and WSe2) is lower than that of graphene and its analogues. *Chem. - A Eur. J.* **20**, 9627–9632 (2014).

51. Chia, H. L., Latiff, N. M., Sofer, Z. & Pumera, M. Cytotoxicity of Group 5 Transition Metal Ditellurides (MTe2; M=V, Nb, Ta). *Chem. - A Eur. J.* **24**, 206–211 (2018).

52. Latiff, N. M., Sofer, Z., Fisher, A. C. & Pumera, M. Cytotoxicity of Exfoliated Layered Vanadium Dichalcogenides. *Chem. - A Eur. J.* **23**, 684–690 (2017).

53. Chen, W. *et al.* Direct Assessment of the Toxicity of Molybdenum Disulfide Atomically Thin Film and Microparticles via Cytotoxicity and Patch Testing. *Small* **14**, 1–7 (2018).

54. Chng, E. L. K., Sofer, Z. & Pumera, M. MoS2 exhibits stronger toxicity with increased exfoliation. *Nanoscale* **6**, 14412–14418 (2014).

55. Van Der Zande, A. M. *et al.* Grains and grain boundaries in highly crystalline monolayer molybdenum disulphide. *Nat. Mater.* **12**, 554–561 (2013).

56. Chen, X. *et al.* CVD-grown monolayer MoS 2 in bioabsorbable electronics and

biosensors. *Nat. Commun.* **9**, 1–12 (2018).

57. Creighton, J. R. & Ho, P. *Introduction to Chemical Vapor Deposition (CVD)*. (2001).

58. Shi, Y. *et al.* Na-assisted fast growth of large single-crystal MoS2 on sapphire. *Nanotechnology* **30**, (2019).

59. Xu, H. *et al.* Control of the nucleation density of molybdenum disulfide in large-scale synthesis using chemical vapor deposition. *Materials (Basel).* **11**, (2018).

60. Chen, F. & Su, W. The effect of the experimental parameters on the growth of MoS2 flakes. *CrystEngComm* **20**, 4823–4830 (2018).

61. Yue, R. *et al.* Nucleation and growth of WSe 2 : enabling large grain transition metal dichalcogenides. *2D Mater.* **4**, (2017).

62. Fu, D. *et al.* Molecular Beam Epitaxy of Highly Crystalline Monolayer Molybdenum Disulfide on Hexagonal Boron Nitride. (2017). doi:10.1021/jacs.7b05131

63. Zhang, Y. *et al.* Direct observation of the transition from indirect to direct bandgap in atomically thin epitaxial $MoSe_2$. *Nat. Nanotechnol.* | **9**, (2014).

64. Han, Z. J., Murdock, A. T., Seo, D. H. & Bendavid, A. Recent progress in plasma-assisted synthesis and modification of 2D materials. *2D Materials* **5**, (2018).

65. Backes, C. *et al.* Guidelines for exfoliation, characterization and processing of layered materials produced by liquid exfoliation. *Chem. Mater.* **29**, 243–255 (2017).

66. Wang, M. *et al.* Surface Tension Components Ratio: An Efficient Parameter for Direct Liquid Phase Exfoliation. *ACS Appl. Mater. Interfaces* **9**, 9168–9175 (2017).

67. Shen, J. *et al.* Liquid Phase Exfoliation of Two-Dimensional Materials by Directly Probing and Matching Surface Tension Components. (2015). doi:10.1021/acs.nanolett.5b01842

68. Backes, C. *et al.* Production of Highly Monolayer Enriched Dispersions of Liquid-Exfoliated Nanosheets by Liquid Cascade Centrifugation. *ACS Nano* **10**, (2016).

69. Raman Scattering in Fluorescence Emission Spectra | Common Errors. Available at: https://www.edinst.com/us/blog/raman-scattering-blog/. (Accessed: 30th October 2019)

70. Princeton Instruments - General Raman. Available at:

https://www.princetoninstruments.com/applications/raman-gen. (Accessed: 30th October 2019)

71. Wagner, R., 309, M. ~, Wagner, R., Raman, A. & Moon, R. *0th International Conference on Wood & Biofiber Plastic Composites ~ Transverse Elasticity of Cellulose Nanocrystals Via atomic Force microscopy*.

72. Promega. RealTime-Glo™ MT Cell Viability Assay - Technical Manual. 1–20 (2016).

73. Promega. CellTox™ Green Cytotoxicity Assay. **1**, 1–22 (2015).

74. Bernal, M. M. *et al.* Luminescent transition metal dichalcogenide nanosheets through one-step liquid phase exfoliation. *2D Mater.* **3**, 1–11 (2016).

75. Yumigeta, K. *et al. Synthesis of metallic MoTe2 nanosheets through high-pressure sputtering: Phase anomaly*.

76. Yamamoto, M. *et al.* Strong enhancement of Raman scattering from a bulk-inactive vibrational mode in few-layer MoTe2. *ACS Nano* **8**, 3895–3903 (2014).

77. Ruppert, C., Aslan, O. B. & Heinz, T. F. Optical properties and band gap of single- and few-layer MoTe2 crystals. *Nano Lett.* **14**, 6231–6236 (2014).

78. Wu, B. *et al.* Differential influence of molybdenum disulfide at the nanometer and micron scales in the intestinal metabolome and microbiome of mice. *Environ. Sci. Nano* **6**, 1594–1606 (2019).